EUROPEAN SPACE AGENCY

ESA Reference: ESA AO/1-11038/21/I-DT

ESA Contract Number: 4000139605/22/I-DT

Project AFRI4Cast - Food Security and Safety In Africa
WP100 - D3 - State-of-the-art review report on the EO analysis methods and algorithms

Submitted by:

SAPIENZA
UNIVERSITÀ DI ROMA

In collaboration with:

AgroApps

SAPIENZA
UNIVERSITÀ DI ROMA

gmv
INNOVATING SOLUTIONS

2 May 2023

Document Information

ESA Contract Number	4000139605/22/I-DT		**Acronym**	AFRI4CAST
Full Title	EO AFRICA EXPLORERS – EXPRO+ Food Security and Safety In Africa			
Start Date	26th October 2022		**Duration**	24 months
Project URL	www.afri4cast.org			
Deliverable	D3 - State-of-the-art review report on the EO analysis methods and algorithms			
Work Package	WP100			
Date of Delivery	**Contractual**		**Actual**	Contractual
Nature	Report		**Dissemination Level**	Confidential
Lead Beneficiary	SIA			
Responsible Author	Professor Giovanni Laneve			
Contributions from	AgroApps, GMV			

Document History

Version	Issue Date	Pages	Changes
V1	22/02/2023	79	
V2	02/05/2023	79	

Disclaimer

Contents

1. Introduction

1.1. Purpose – Scope

The objective of the AFRI4Cast project is to develop a modeling platform making full exploitation of satellite remote sensing of PRISMA and ECOSTRESS sensors for climate change impact analyses on agriculture, and making it available to African stakeholders for shaping future agricultural policies in the African Continent. This modeling solution will be a discrete simulation engine where different EO processing techniques and tested crop and disease models are integrated in order to carry out high temporal and spatial analysis simulations for the goal of food safety and security.

The models will employ most of the available data and products of both the ECOSTRESS and the PRISMA missions. However, in the context of remote sensing for agriculture, those 2 sensors can not contribute much due to their limited crop monitoring capabilities, at crop parcel scale, which is attributed to their low spatial and temporal resolution. As far as EO data is concerned, AFRI4CAst will deliver a remote sensing infrastructure for acquisition, reprocessing , vegetation feature indices calculation and biophysical parameters estimation.

The infrastructure will incorporate an algorithmic chain appropriate for EO data fusion for resolution enhancement and elaboration to increase the level of detail at which resulting indices and products can be extracted. Super-resolution neural network architectures will be trained using archived acquisitions to improve the spatial resolution of PRISMA hyperspectral data and temporal resolution of ECOSTRESS products.
The overall aims of the “D3: State-of-the-art review report on the EO analysis method/s & algorithm/s ” are :

- to list and describe the major EO products that will be used throughout the project, as input data sources to the fusion algorithms in order to provide the enhanced thermal and hypespectral EO data services
- to provide documentation for the EO data requirements, for the accomplishment of the Data Fusion and the Modeling tasks
- to present a scientific review report of the state of the art EO analysis methods and algorithms that exist for the tasks of data fusion on thermal & hyperspectral data, Radiative Transfer Model Inversion, Crop Monitoring, and conclude on which approach will be tested and applied throughout the project.

2. Terms, Definitions and Abbreviations

Table of Acronyms

ADS	Annotation DataSet
ALEXI	Atmosphere-Land Exchange Inverse
ASI	Italian Space Agency
BOA	Bottom-of-Atmosphere
CBD	Context-Based Decision
CCC	Canopy Chlorophyll Content
CNMF	Coupled Nonnegative Matrix Factorization
CNN	Convolutional Neural Networks
CONUS	Continental United States

CP	Control Points
CS	Component Substitution
CT	Crop Type
CWC	Canopy Water Content
DIAS	Data and Information Access Service
DisALEXI	Disaggregated ALEXI algorithm
DOY	Day Of Year
DOYM	Day of NDVImax
ECOSTRESS	ECOsystem Spaceborne Thermal Radiometer Experiment on Space Station
EO	Earth Observation
EOS	End of Season
ET	Evapotranspiration
ESA	European Space Agency
ESI	Evaporative Stress Index
EUMETSAT	European organization for the Exploitation of Meteorological Satellites
fAPAR	Fraction of Absorbed Photosynthetically Active Radiation
fCover	Green cover fraction
FVC	Fraction Vegetation Cover
GLP	Gaussian Laplacian Pyramid
GPU	Graphics Processing Unit
GS	Gram Schmidt
GSA	Global Sensitivity Analysis
GSD	Ground Sampling Distance
GSW	Generalised Split-Window
HEG	HDF-EOS To GeoTIFF Conversion Tool
HS	HyperSpectral
IHS	Intensity Hue Saturation
IR	Infrared
ISS	International Space Station
JPL	Jet Propulsion Laboratory
LAI	Leaf Area Index
LE	Latent Heat Flux
LIDF	Leaf Inclination Distribution Function
LSA	Land Surface Analysis
LST	Land Surface Temperature
LUT	Look-up Table
ML	Machine Learning
MLRA	Machine Learning Regression Algorithm
MODIS	Moderate Resolution Imaging Spectroradiometer
MRA	Multiresolution Analysis
MS	MultiSpectral
MSG	Meteosat Second Generation
MSI	MultiSpectral Instrument

MSR	Modified Simple Ratio
MSU	Mass Storage Unit
MWR	Microwave Radiometer
NASA	National Aeronautics and Space Administration
NDVI	Normalized Difference Vegetation Index
NIR	Near-Infrared Radiation
NNET	Neural Network
OLCI	Ocean and Land Colour Instrument
OLI	Operational Land Imager
OZA	Observer Zenith Angle
PAN	Panchromatic
PBC	Phenology-based Classification
PCA	Principal Component Analysis
PHyTIR	Prototype HyspIRI Thermal Infrared Radiometer
PMW	Passive Microwave
PRI	Photochemical Reflectance Index
PRISMA	PRecursore IperSpettrale della Missione Applicativa
PSF	Point Spread Function
PSRI	Plant Senescence Reflectance Index
PWV	Precipitable Water Vapor
REP	Red Edge Position
ResNet	Residual Network
RFR	Random Forest Regression
RMSE	Root Mean Square Error
RTM	Radiative Transfer Model
SAF	Satellite Application Facility
SCL	Scene Classification Layer
SEB	Surface Energy Balance
SEVIRI	Spinning Enhanced Visible and InfraRed Imager
SFIM	Smoothing Filtered-based Intensity Modulation
SIPI	Structural Independent Pigment Index
SL2P	Sentinel-2 Prototype Processor
SLSTR	Sea and Land Surface Temperature Instrument
SMM	Stochastic Mixing Model
SNAP	Sentinel Application Platform
SNR	Signal-to-Noise Ratio
SOS	Start of Season
SRF	Spectral Response Function
SRAL	SAR Radar Altimeter
STC	SpatioTemporal Consistency

STFN	Spatiotemporal Fusion Network
SURF	Speeded-up Robust Feature
SWIR	Short Wave Infrared Radiation
SZA	Sun Zenith Angles
TES	Temperature and Emissivity Separation
TIR	Thermal Infrared Radiation
TIRS	Thermal Infrared Sensor
TOC	Top of Canopy
TsHARP	Thermal Sharpening Algorithm
USDA	United States Department of Agriculture
VNIR	Visible Near Infrared Radiation

3. Input data products for AFRI4Cast EO Services

3.1. ECOSTRESS

3.1.1. Mission

The ECOsystem Spaceborne Thermal Radiometer Experiment on Space Station (ECOSTRESS) mission is devoted to the collection of measurements regarding the temperature of plants in order to improve the comprehension about their water needs as well as their response to changes in water availability. ECOSTRESS was launched to the International Space Station (ISS) on the 29th of June 2018 and was installed on the 3rd of July 2018 (Hulley et al., 2022). Continuous measurements are collected by ECOSTRESS between 52°N and 52°S at various times of the day with a daily overpass return frequency for any same spot on Earth, dependent on the latitude. ECOSTRESS gathers observations over the continental U.S. (CONUS) as well as over key biomes, agricultural zones and selected FLUXNET validation sites worldwide within its viewing swath width of 384km.

ECOSTRESS carries a thermal radiometer called Prototype HyspIRI Thermal Infrared Radiometer (PHyTIR) created by National Aeronautics and Space Administration (NASA)'s Jet Propulsion Laboratory (JPL). PHyTIR observes over five bands from 8 to 12.5 μm wavelengths within the Thermal Infrared Radiation (TIR) spectrum and a supplementary sixth band at 1.6 μm in the Short Wave Infrared Radiation (SWIR) spectrum (Table 1.) exploited for cloud detection (Fisher et al., 2020). According to Hulley et al. (2022), ECOSTRESS provides at present the highest spatial resolution spaceborne TIR data as the spatial resolution at nadir is 69 m x 38 m, which is resampled to 70 m x 70 m by the ECOSTRESS data production software aiming to reduce noise and facilitate the data use (Fisher, 2018a)

Table 1. ECOSTRESS Spectral Bands (Reference:https://lpdaac.usgs.gov/data/get-started-data/collection-overview/missions/ecostress-overview/)

Band	Emitted Range (band center, μm)	Band Notes
1	1.66	
2	8.285	Unavailable for acquisitions after May 15, 2019
3	8.785	
4	9.06	Unavailable for acquisitions after May 15, 2019
5	10.522	
6	12.001	

3.1.2. Data products

The ECOSTRESS mission produces distributable swath, gridded and tiled science data products. The products depict four levels of data processing, with each level integrating additional information, plus Level-0 products that correspond to the raw collected telemetry. According to Hook Simon and the ECOSTRESS Team (2017) each processing level refers to:

- **Level-1:** Calibrated geolocated radiances
- **Level-2:** Land Surface Temperature and emissivity data acquired from the Level-1 radiance data as well as cloud mask products.
- **Level-3:** Evapotranspiration products retrieved from Level-2 data.
- **Level-4:** Water Use Efficiency and Evaporative Stress Index products derived from Level-3 data.

Within the context of AFRI4Cast, the below described ECOSTRESS science data products shall be used (Table 2.):

- **ECO1BGEO:** The ECO1BGEO Version 1 data product offers geolocation information for the radiance values. This data product should be used for the georeference of ECO2CLD, ECO2LSTE, ECO3ANCQA, ECO3ETPTJPL, ECO4ESIPTJPL, and ECO4WUE data products. ECO1BGEO is provided as swath data in HDF5 file format in a spatial resolution of 70m and a daily temporal resolution. The ECO1BGEO data product consists of data layers for latitude and longitude values, surface height, solar and view geometry information and the fraction of pixel on land versus water (Smyth and Leprince, 2018)
- **ECO2CLD.001**: The ECO2CLD Version 1 data product provides a cloud mask layer (Hulley and Hook, 2018a) in order to determine the cloud coverage for the ECO2LSTE, ECO3ETPTJPL, ECO4ESIPTJPL, and ECO4WUE data products. ECO2CLD is provided in HDF5 file format in a spatial resolution of 70 m and the ECO1BGEO product is required for its georeferenced.
- **ECO2LSTE.001:** The ECO2LSTE Version 1 data product provides atmospherically corrected land surface temperature and emissivity values obtained from five thermal infrared (TIR) bands. The physics-based Temperature and Emissivity Separation (TES) algorithm was used to create the ECO2LSTE data product (Hulley and Hook, 2018b). The ECO2LSTE data product is distributed as swath data in HDF5 file format in a spatial resolution of 70m and a daily temporal resolution, while the ECO1BGEO product is additionally required for its georeference. This data product is comprised of layers of LST, LST error, emissivity for bands 1 through 5, emissivity error for bands 1 through 5, quality control for LST and emissivity, wideband emissivity and Precipitable Water Vapor (PWV). Due to an anomaly in the primary mass storage unit (MSU) of ECOSTRESS, data acquisitions after the 15th of May 2019 contain data values only for the TIR bands 2, 4 and 5, whereas TIR bands 1 and 3 contain fill values to facilitate direct data streaming from the ISS.
- **ECO3ETALEXI.001:** The ECO3ETALEXI Version 1 data product, provided by NASA's JPL, offers daily estimates of evapotranspiration (ET) using the Level-2 ECOSTRESS LST and emissivity product (ECO2LSTE) together with supplementary meteorological data and other spaceborne vegetation cover information. ECO3ETALEXI data product is obtained using the Atmosphere Land Exchange Inverse (ALEXI) Disaggregation algorithm (DisALEXI) (Cawse-Nicholson and Anderson, 2021a) a physics-based surface energy balance (SEB) algorithm (Anderson et al., 2021). This data product is distributed in

HDF5 file format in a spatial resolution of 70m and a daily temporal resolution. ECO3ETALEXI contains daily ET and ET uncertainty layers as well as the correspondent quality flags.

- **ECO3ETPTJPL.001:** The ECO3ETPTJPL Version 1 data product provides daily estimates of evapotranspiration (ET) according to the Priestly-Taylor Jet Propulsion Laboratory (PT-JPL) algorithm (Fisher, 2018a). This data product is distributed in HDF5 file format in a spatial resolution of 70m and a daily temporal resolution. ECO3ETPTJPL contains instantaneous and daily ET layers as well as layers regarding the canopy transpiration, soil evaporation, interception evaporation and ET uncertainty.
- **ECO4ESIALEXI.001:** The ECO4ESIALEXI Version 1 data product, provided by NASA's JPL, offers estimates of the Evaporative Stress Index (ESI) which is calculated based on the relative daily evapotranspiration (ET) fraction derived from ECOSTRESS Level-3 product daily ET estimates. ECO3ETALEXI data product is obtained using the Atmosphere Land Exchange Inverse (ALEXI) Disaggregation algorithm (DisALEXI) (Cawse-Nicholson and Anderson, 2021b). This data product is distributed in HDF5 file format in a spatial resolution of 70 m and it contains layers of daily ESI, ESI uncertainty and the correspondent quality flags.
- **ECO4ESIPTJPL.001:** The ECO4ESIPTJPL Version 1 data product provides estimates of the Evaporative Stress Index (ESI) obtained based on the Priestly-Taylor Jet Propulsion Laboratory (PT-JPL) algorithm (Fisher, 2018b). ECO4ESIPTJPL contains layers of ESI and potential ET while it is distributed in HDF5 file format in a spatial resolution of 70 m.
- **ECO4WUE.001:** The ECO4WUE Version 1 data product provides Water Use Efficiency (WUE) data calculated based on the Priestly-Taylor Jet Propulsion Laboratory (PT-JPL) algorithm (Fisher, 2018c). ECO4WUE data product consists of a single layer of water use efficiency and it is distributed in HDF5 file format in a spatial resolution of 70 m.

Table 2. ECOSTRESS science data products' features.

Product	Description	Spatial Resolution (m)	Temporal Resolution	Temporal Extent	Reference
ECO1BGEO	Geolocation	70	Daily	09-07-2018 to Present	(Smyth and Leprince, 2018)
ECO2CLD.001	Cloud Mask	70	Daily	09-07-2018 to Present	(Hulley and Hook, 2018a)
ECO2LSTE.001	Land Surface Temperature (LST) and Emissivity	70	Daily	09-07-2018 to Present	(Hulley and Hook, 2018b)

ECO3ETALEXI.001	Evapotranspiration (ET)	70	Daily	15-07-2018 to Present	(Cawse-Nicholson and Anderson, 2021a)
ECO3ETPTJPL.001	Evapotranspiration (ET)	70	Daily	15-07-2018 to Present	(Fisher, 2018a)
ECO4ESIALEXI.001	Evaporative Stress Index (ESI), Evapotranspiration (ET)	70	Daily	15-07-2018 to Present	(Cawse-Nicholson and Anderson, 2021b)
ECO4ESIPTJPL.001	Evaporative Stress Index (ESI), Evapotranspiration (ET)	70	Daily	15-07-2018 to Present	(Fisher, 2018a)
ECO4WUE.001	Water Use Efficiency (WUE)	70	Daily	15-07-2018 to Present	(Fisher, 2018b)

Referring to the naming conventions of ECOSTRESS filenames (https://lpdaac.usgs.gov/data/get-started-data/collection-overview/missions/ecostress-overview/), in an example of a grid product the filename ECOv002_L2G_LSTE_24423_017_20221026T195702_0710_01.h5 indicates:

- ECO – Sensor
- v002 – Product Version
- L2G – Processing Level and Type (Blank for Swath or G = Grid)
- LSTE – Geophysical Parameter
- 24423 – Orbit Number
- 017 – Scene ID
- 20221026 – Date of Acquisition (YYYYMMDD)
- T195702 – Time of Acquisition (HHMMSS) (in UTC)
- 0710 – Build ID of software that generated product, Major+Minor (2+2 digits)
- 01 – Product Iteration Number
- .h5 – Data Format for Grid or Swath

Regarding the data access, the following services and API provide users with the ability to search, query, discover, visualize, transform and download ECOSTRESS data products:

- USGS EarthExplorer: https://earthexplorer.usgs.gov/

- NASA Earthdata:https://search.earthdata.nasa.gov/search?q=C1534729776-LPDAAC_ECS
- LP DAAC Data Pool: https://e4ftl01.cr.usgs.gov/ECOSTRESS/
- OPeNDAP API
- AppEEARS tool API: https://appeears.earthdatacloud.nasa.gov/task/area.

3.2. PRISMA

3.2.1. Mission

PRISMA (PRecursore IperSpettrale della Missione Applicativa) is a hyperspectral satellite system launched by the Italian Space Agency (ASI) on 22 March 2019, into a low-Earth, sun-synchronous orbit at 615 km altitude, with a repeat cycle of 29 days and a revisit capability for a specific target of less than one week with off-nadir viewing. It is classified as a small satellite with a 5-year estimated operational life. The instruments combine two hyperspectral sensors and one panchromatic camera. Two hyperspectral sensors can capture images in a continuum of 239 spectral bands ranging from 400 to 2500 nm, 66 in the VIS-NIR, and 173 in the SWIR spectrum, with a spectral resolution smaller than 12 nm and a spatial resolution of 30 m (Guarini et al., 2018). The panchromatic camera has a GSD of 5 m and works in the spectral range of 400–700 nm. The recorded images were in an area of interest spanning from 180° W to 180° E longitude and 70° S to 70° N latitude (R. Loizzo et al., 2018).

3.2.2. Data products

The following standard processing level products are available for PRISMA:

- **L1 product:** The L1 Earth Observation Product basically contains four kinds of data organized in four layers: two Radiometrically Calibrated HYPER and PAN Surface_Obs cubes and two Co-registered HYPER and PAN Surface_Obs cubes. It also contains the Cloud Coverage, Sun Glint and Generic Land Cover masks. Coregistered cubes correspond to the Radiometric Cubes where also spatial co-registration of SWIR and PAN with respect to VNIR channel is performed. It has been dedicated to send both not-co-registered and co-registered data, since co-registration is founded on interpolation so co-registered data represent manipulated data. Not co-registered data instead is directly associable to L0a Raw Data, simply the Radiance transformation is applied.

- **L2 product (L2B, L2C and L2D):** The Level 2 processing is in charge of processing Top-of-Atmosphere spectral radiance measurements into geophysical parameters. These parameters depend on the observed pixels and provide information on the at-surface radiance/reflectance (L2B/L2C) and the properties of the atmosphere above the surface (Guarini et al., 2018):

- Aerosol Optical Thickness and Angstrom Exponent;
- Water Vapour;
- Thin Cloud Optical Thickness.

L2D product results from the orthorectification of the L2C level image.

Occasionally, PRISMA images geolocation error could reach values of 3 – 5 pixels (90m – 150m). In order to improve the image geolocation, a pre-processing procedure has been introduced with the use of a Python package based on AROSICS algorithm which co-registers PRISMA images on Sentinel-2 imagery (Scheffler et al., 2017). A procedure has been also developed for effectively improving the PRISMA spatial resolution to 10 or 20m spatial resolution by using Sentinel-2 imagery as proposed by Acito et al. (2022). The panchromatic band is not used for sharpening because the high resolution band do not cover the whole spectral region of interest.

Regarding the access on PRISMA data, PRISMA images can be downloaded from the ASI portal: https://prisma.asi.it/. A registration is requested and both archived data and new acquisition can be requested through the account. Images are delivered in HDF-EOS5 format (.he5). Different programs are available to convert hdf data in geotiff:

- a tool in R named prismaread (https://irea-cnr-mi.github.io/prismaread/);
- a tool of the commercial software called ENVI (ENvironment for Visualizing Images);
- a plug-in for QGIS named EnMAP-box
- a tool in Python, (prisma2geotiff.py).

All tools divide the image in three data cubes:

- VNIR Cube containing 66 spectral bands;
- SWIR Cube containing 173 spectral bands;
- PAN Cube containing 1 panchromatic band at 5 m spatial resolution.

Table 3. shows a list of indices (from EnMAP toolbox) capable to characterize vegetation bio-physical conditions. A very comprehensive list of spectral indices developed for vegetation characterization is given at https://www.indexdatabase.de/db/i.php.

Table 3. Selection of vegetation indices which can be potentially computed by using an hyperspectral sensor.

Characteristic	Spectral indices
Structure	NDVI, MCARI, MSAVI, MTVI, OSAVI, SPVI, RDVI
Chlorophyll	CSI, Greenness Index, GM, NPQI, PRI, Red Edge, SR705, TCARI, TVI, Vogelmann Index, ZTM, SR, PSSR, LCI, MLO, MSR
Carotenoids and Anthocyanin	ARI, CRI, PSSRc, SIPI
Leaf Water	DSWI, LWVI, MSI, NDWI, PWI, SRWI
Dry Matter	SWIRV1, CAI, NDLI, NDNI, BGI, BRI, RGI, SRPI, NPCI, PSRI
Fluorescence	CUR, LIC

The formulas to compute the indices listed in Table 3. are given in Appendix 1. The list of PRISMA spectral channels is given in Appendix 2.

3.3. MODIS

3.3.1. Mission

Moderate Resolution Imaging Spectroradiometer (MODIS) is a key instrument aboard two NASA satellites, Terra and Aqua, which were launched in 1999 and 2022, respectively. The design of the instrument combines features of the radio meter Advanced Very High Resolution Radiometer (AVHRR) and Landsat Thematic Mapper and works in medium and long infrared (IR) spectral bands (Justice et al., 1998). MODIS is capable of receiving data in 20 reflective solar bands (RSB) and in 16 bands of thermal (thermal emissive bands-TEB) radiation of the infrared zone of electromagnetic spectrum with their wavelengths ranging from 0.41 to 2.2 μm and from 3.75 to 14.24 μm, respectively, providing observations in spatial analysis of 250 m for bands 1-2, 500 m for bands 3-7 and of 1 km for bands 8-36 (Xiong et al., 2009) with a revisit period of 1-2 days.

3.3.2. Data products

In terms of AFRI4Cast, MODIS Land Surface Temperature and Emissivity as well as MODIS Evapotranspiration data products will be used (Table 4.).

- **MOD11A1.061:** The MOD11A1 Version 6.1 Level-3 product acquired from MODIS/Terra provides daily gridded Land Surface Temperature (LST) and Emissivity measurements at a global scale in a spatial resolution of 1 km. The MOD11A1 product data set includes layers of LST day and night, emissivity, quality control for daytime and nighttime LST and emissivity, time of the daytime and nighttime LST observation and the view zenith angle of daytime and nighttime LST (Wan, 2006).
- **MOD16A2.061:** The MOD16A2 Version 6.1 Level-4 product acquired from MODIS/Terra provides gridded Net Evapotranspiration/Latent Heat Flux measurements at a daily pace in an 8-day composite in a special resolution of 500 m. MOD16A2's production algorithm is established in the sense of Penman-Monteith equation in which daily meteorological data as well as other MODIS data products are used as input (Running, S.W. et al., 2019). MOD16A2 includes layers referring to the composited ET, potential ET, Latent Heat Flux (LE), potential LE as well as a quality control layer.

MOD11A1 and MOD16A2 are distributed in HDF-EOS file format, while its naming convention follows the structure: e.g., MOD11A1.A2000185.h25v03.006.2006299173851.hdf where:

- MODD11A1 – MODIS Product short name
- A2000185 – Julian Date of Acquisition (A-YYYYDDD)
- h25v03 – Tile identifier (Tile location- horizontalXXverticalYY)
- 006 – Collection Version
- 2006299173851 - Julian Date of Production (YYYYDDDHHMMSS)
- .hdf – Data format (HDF-EOS)

Table 4. MODIS data products' features.

Product	Description	Spatial Resolution (m)	Temporal Resolution	Temporal Extent	Reference
MOD11A1	Land Surface Temperature (LST) and Emissivity	1000	Daily	24-02-2000 to Present	(Wan,2006)
MOD16A2	Evapotranspiration /Latent Heat Flux	500	8-day composite	01-01-2001 to Present	(Running, S.W. et al., 2019)

Regarding the data access, the following services and API provide users with the ability to freely search, query, discover, visualize and download the above mentioned data products:

- USGS EarthExplorer: https://earthexplorer.usgs.gov/
- Earthdata: https://lpdaac.usgs.gov/tools/earthdata-search/
- LP DAAC Data Pool: https://e4ftl01.cr.usgs.gov/MOLT/
- OPeNDAP API
- MODIStsp R package

With reference to the processing of MODIS data products raster time series, MODIStsp R package facilitates the preprocessing operations, i.e., downloading, mosaicking, stacking, resizing and reprojecting (Busetto and Ranghetti, 2018). MODIStsp required inputs are comprised of MODIS data products HDF files, which will afterwards be preprocessed according to user's choices. The output layers are produced and saved as single-band rasters matching the acquisition date available for the desired MODIS data product within the specified time period. Likewise, the HDF-EOS To GeoTIFF Conversion Tool (HEG) is a tool that targets on assisting the reformatting, reprojection, mosaicking and subsetting procedures on HDF-EOS data products. HEG supports MODIS (Terra and Aqua) data products along with several remotely sensed datasets. HEG TIFF output files are ingestible into commonly used GIS applications (https://hdfeos.org/software/heg.php).

3.4. Copernicus Sentinel-2 & Sentinel-3

3.4.1. Sentinel-2

The Sentinel-2 mission consists of a constellation of two polar-orbiting satellites that are phased at 180° degrees from one another and placed in the same orbit. Its wide sweep width and high revisit time (10 days with one satellite at the equator and 5 days with two satellites under cloud-free circumstances, resulting in 2-3 days at mid-latitudes) support monitoring of vegetation changes throughout the growing season. The S2A and S2B Sentinel-2 satellites were launched in June 2015 and March 2017, respectively. The range of latitudes that are covered is from 56° S to 84° N. Sentinel-2 is equipped with a MultiSpectral Instrument (MSI), which passively collects the reflected sunlight from the Earth while the satellite moves along its orbital path. Sentinel-2 provides observations at 12 different spectral bands in three possible spatial resolutions, varying from 10 to 60m (Table 5.) (https://sentinel.esa.int/web/sentinel/missions/sentinel-2/instrument-payload/resolution-and-swath).

Table 5. Wavelengths and Bandwidths of the three Spatial Resolutions of the Sentinel-2 MSI instrument.

Spatial Resolution (m)	Band Number	S2A		S2B	
		Central Wavelength (nm)	Bandwidth (nm)	Central Wavelength (nm)	Bandwidth (nm)
10	2	492.4	66	492.1	66
	3	559.8	36	559	36
	4	664.6	31	664.9	31
	8	832.8	106	832.9	106
20	5	704.1	15	703.8	16

	6	740.5	15	739.1	15
	7	782.8	20	779.7	20
	8a	864.7	21	864	22
	11	1613.7	91	1610.4	94
	12	2202.4	175	2185.7	185
60	1	442.7	21	442.2	21
	9	945.1	20	943.2	21
	10	1373.5	31	1376.9	30

Products from Sentinel-2 consist of elementary granules with a single orbit and a defined size. The smallest, indivisible portion of a product is called a granule (containing all possible spectral bands). Specifically, the granules, also known as tiles, for Level-1C and Level-2A products are 100x100 km^2 ortho-images in UTM/WGS84 projection and range in size from 700 to 1000 MB. The 60 zones that make up the Earth's surface are determined by the UTM (Universal Transverse Mercator) system, while each UTM zone has a vertical longitude width of 6° and a horizontal latitude width of 8°. Tiles can be entirely or partially covered by image data as partially covered tiles match those along the edge or top/bottom of the Datastrip. Within the context of AFRI4Cast, Sentinel-2 MSI Level 2A products will be used, which correspond to the Bottom-of-Atmosphere (BOA) reflectance in cartographic geometry for the selected areas.

Sentinel-2 Level 2A products are distributed in SAFE file format following the below mentioned naming convention:

MMM_MSIXXX_YYYYMMDDHHMMSS_Nxxyy_ROOO_Txxxxx_<Product Discriminator>.SAFE

where,
MMM: is the mission ID (S2A/S2B)
MSIXXX: Product Level. MSIL1C denotes the Level-1C product level/ MSIL2A denotes the Level-2A product level
YYYYMMDDHHMMSS: the datatake sensing start time
Nxxyy: the PDGS Processing Baseline number (e.g. N0204)
ROOO: Relative Orbit number (R001 - R143)
Txxxxx: Tile Number field
SAFE: Product Format (Standard Archive Format for Europe)

Data access to Sentinel-2 Level 2A products is free and it can be granted via Copernicus Open Access Hub. Sentinel-2 data products are also available via cloud in the Copernicus Data and Information Access Service (DIAS) cloud environments, e.g. ONDA, CREODIAS. By July 2023, Sentinel-2 data products will be also accessible through the Copernicus Data Space Ecosystem, in which data accessibility via API will be provided as well.

3.4.2. Sentinel-3

Sentinel-3, a European Earth Observation satellite mission operated by ESA and EUMETSAT, was created to support Copernicus ocean, land, atmospheric, emergency, security and cryospheric applications. Aiming to support ocean forecasting systems, environmental monitoring and climate monitoring, the primary goal of the Sentinel-3 mission is to assess sea surface topography, sea and land surface temperature and ocean and land surface color with high precision and reliable measurements. Sentinel-3 is equipped with four main instruments:

- OLCI: Ocean and Land Colour Instrument
- SLSTR: Sea and Land Surface Temperature Radiometer
- SRAL: SAR Radar Altimeter
- MWR: Microwave Radiometer.

The two in-orbit Sentinel-3 satellites, S3A and S3B, enable a short revisit time of less than two days for OLCI and less than one day for SLSTR at the equator.

Within AFRI4Cast, SLSTR products could be used, which are created separately for the two views of the instrument (nadir and oblique) at a spatial resolution that depends on the used channel i.e., 500 m resolution for the solar reflectance bands (S1-S6) and 1 km resolution for the thermal infrared bands (S7-S9 and F1-F2) (Table 6.). Specifically, the SLSTR thermal bands (the three infra-red channels S7, S8 and S9 at 3.74 μm, 10.85 μm and 12 μm) are used for the retrieval of LST products (https://sentinels.copernicus.eu/web/sentinel/user-guides/sentinel-3-slstr/overview/geophysical-measurements/land-surface-temperature). SLSTR Level-2 Land Surface Temperature (LST) data products aim to provide an alternative source for LST measurements in terms of AFRI4Cast, except from the MODIS LST ones.

Table 6. The radiometric bands of the SLSTR instrument.

Band	Central Wavelength (nm)	Bandwidth (nm)	Function	Comments		Resolution (m)
S1	554.27	19.26	Cloud screening, vegetation monitoring, aerosol	VNIR	Solar Reflectance Bands	500
S2	659.47	19.25	NDVI, vegetation monitoring, aerosol			
S3	868	20.6	NDVI, cloud flagging, Pixel co-registration			
S4	1374.8	20.8	Cirrus detection over land	SWIR		
S5	1613.4	60.68	loud clearing, ice, snow, vegetation monitoring			
S6	2255.7	50.15	Vegetation state and cloud clearing			
S7	**3742**	**398**	**SST, LST, Active fire**	**Thermal IR Ambient bands (200 K -320 K)**		1000
S8	**10854**	**776**	**SST, LST, Active fire**			
S9	**12022.5**	**905**	**SST, LST**			

F1	3742	398	Active fire	Thermal IR fire emission bands	
F2	10854	776	Active fire		

SLSTR Level-2 LST product provides gridded land surface parameters at a spatial resolution of 1 km. It is comprised of measurements with LST values which are provided for each re-gridded or orphan pixel along with the corresponding auxiliary parameters. One Annotation DataSet (ADS) is specifically related to LST MD and offers for each gridded pixel and orphan pixel:

- Normalised Difference Vegetation Index (NDVI)
- GlobCover surface classification code (noted biome)
- Fractional vegetation cover
- Total column water vapour

Nine files with annotations derived from the Level-1 product are also included in this product. Each ADS included in the Level-1B product, related to the 1 km grid and the nadir view or associated with the tie-point grid, is replicated as an ADS in this product, with the exception of the quality ADS: Cartesian_in, Cartesian_tx, Flags_in, Geodetic_in, Geodetic_tx, Geometery_tn, Indices_in, Met_tx,Time_im

The SLSTR files are collected into a SAFE container. Level-1 and 2 products are enclosed in NetCDF 4 product files. The file naming convention of SLSTR products is identified by the fields described below:

MMM_SL_L_TTTTTT_yyyymmddThhmmss_YYYYMMDDTHHMMSS_YYYYMMDDTHHMMSS_[instance ID]_GGG_[class ID].SEN3

where:
MMM: mission ID (S3A/S3B, S3_ = for both SENTINEL-3A and 3B)
S: the data source/consumer (SL = SLSTR)
L: the processing level (0/1/2)
TTTTTT: the data Type ID
  Level 0 SLSTR data:
    "SLT___" = ISPs.
  Level-1 SLSTR data:
    "RBT___" = TOA Radiances and Brightness Temperature
    "RBT_BW" = browse product derived from "RBT___".
  Level-2 SLSTR data:
    "WCT___" = 2 and 3 channels SST for nadir and along track view
    "WST___" = L2P sea surface temperature
    "LST___" = land surface temp
    "FRP___" = Fire Radiative Power
    "WST_BW" = browse product derived from "WST___"
    "LST_BW" = browse product derived from "LST___".
YyyymmddThhmmss: the sensing start time
YYYYMMDDTHHMMS: the sensing stop time

YYYYMMDDTHHMMSS: the product creation date
[instance ID] consists of 17 characters, either uppercase letters or digits or underscores "_"
GGG: identifies the centre which generated the file
[class ID]: dentifies the class ID for instrument data products with conventional sequence P_XX_NNN

Data access to SLSTR Level-2 Land Surface Temperature (LST) data products is free and it can be granted via Copernicus Open Access Hub. Sentinel-2 data products are also available via cloud in the Copernicus Data and Information Access Service (DIAS) cloud environments, e.g. ONDA, CREODIAS. By July 2023, Sentinel-3 data products will be also accessible through the Copernicus Data Space Ecosystem, in which data accessibility via API will be provided as well.

3.5. Landsat 8 & 9

3.5.1. Missions

Landsat 8 & 9 are Earth observation satellites operated by NASA that launched on the 11th of February 2013 and on 27th of September 2021, respectively. The Operational Land Imager (OLI) and the Thermal Infrared Sensor (TIRS) are the two scientific instruments that comprise the payload of Landsat 8 satellite. With a spatial resolution of 30 meters (visible, NIR, SWIR), 100 meters (thermal) and 15 meters (panchromatic) (Table 7.) and a temporal resolution of 16 days, these OLI and TIRS sensors offer seasonal coverage of the global landmass. Landsat 9 is equipped with the Operational Land Imager 2 (OLI-2) and the Thermal Infrared Sensor 2 (TIRS-2). In the visible, near-infrared, and shortwave infrared regions of the electromagnetic spectrum, OLI-2 collects data with a spatial resolution of 30 m for the multispectral bands and 15 m for the panchromatic band and a wide image swath of 185 km. OLI-2 is replicating the Landsat 8's OLI regarding the spectral, spatial, radiometric and geometric qualities. The Thermal Infrared Sensor 2 (TIRS-2) on Landsat 9 uses the same quantum physics-based technology as the TIRS on Landsat 8 in order to measure emissions of infrared energy. It measures land surface temperature in two thermal infrared bands. In terms of instrument class and stray light reduction, TIRS-2 is an upgraded version of Landsat 8's TIRS.

OLI and OLI-2 gather information in the visible, near-infrared, short wave infrared and panchromatic spectral bands while TIRS and TIRS-2 collect data for two more narrow thermal infrared spectral bands, which were previously covered by one wide spectral band on Landsats 4-7. According to the specifications, TIRS gathers image data over a 185 km swath for the two thermal infrared spectral bands with a spatial resolution of 100 m. The two bands, which are an improvement over the single-band thermal data collected by previous Landsat satellites (the ETM + and TM sensors collect data for a 10.0-12.5 m thermal band), were chosen to enable atmospheric correction of the thermal data using a split-window algorithm (https://landsat.gsfc.nasa.gov/satellites/landsat-8/spacecraft-instruments/thermal-infrared-sensor/tirs-requirements/).

Table 7. Landsat 8 & 9 Operational Land Imager (OLI) and Thermal Infrared Sensor (TIRS) radiometric bands.

Bands	Wavelength (micrometers)	Resolution (meters)
Band 1 - Coastal aerosol	0.43-0.45	30

Band 2 - Blue	0.45-0.51	30
Band 3 - Green	0.53-0.59	30
Band 4 - Red	0.64-0.67	30
Band 5 - Near Infrared (NIR)	0.85-0.88	30
Band 6 - SWIR 1	1.57-1.65	30
Band 7 - SWIR 2	2.11-2.29	30
Band 8 - Panchromatic	0.50-0.68	15
Band 9 - Cirrus	1.36-1.38	30
Band 10 - Thermal Infrared (TIRS) 1	10.6-11.19	100
Band 11 - Thermal Infrared (TIRS) 2	11.50-12.51	100

3.5.2. Data products

Landsat Level-2 science products are created from Collection 2 Level-1 inputs that meet the <76 degrees Solar Zenith Angle constraint and include the required auxiliary data inputs to generate a scientifically viable product. Landsat 8/9 Operational Land Imager (OLI) surface reflectance products are generated using the Land Surface Reflectance Code (LaSRC) algorithm (Version 1.5.0).

Within AFRI4Cast, Landsat 8-9 TIRS Collection 2 Level-2 Science products (L2SP) may be used as an alternative thermal data source rather than ECOSTRESS data products. The L2SP include Surface Reflectance and Surface Temperature scene-based products at a spatial resolution of 30 m and a temporal resolution of 3 days. L2SPs are available for the following Landsat 8-9 OLI/TIRS acquisition dates:

- Landsat 8 OLI/TIRS: April 2013 to Present
- Landsat 9 OLI II/TIRS II: January 31, 2022 to Present

Landsat 8-9 data products are distributed in GEOTIFF (.TIF) file format following the below naming convention:

LXSS_LLLL_PPPRRR_YYYYMMDD_yyyymmdd_CC_TX.TIF

where:
L: Landsat
X: Sensor of: C = Combined TIRS and OLI. Indicates which sensor collected data for this product
S: Landsat satellite (08 for Landsat 8, 09 for Landsat 9)
LLLL: Processing level (L2SP, L2SR)
PPP: Satellite orbit location in reference to the Worldwide Reference System-2 (WRS-2) path of the product
RRR: Satellite orbit location in reference to the WRS-2 row of the product
YYYY: Acquisition year of the image
MM: Acquisition month of the image
DD: Acquisition day of the image
yyyy: Processing year of the image
mm: Processing month of the image

dd: Processing day of the image
CC: Collection number (e.g., 02)
TX: Collection category: "T1" for Tier 1 (highest quality), "T2" for Tier 2

Regarding the data access, the U.S. Geological Survey (USGS) provides Landsat 8-9 Operational Land Imager/Thermal Infrared Sensor (OLI/TIRS) Collection 2 Level-2 Science Products (L2SP) through NASA's EarthExplorer or LandsatLook.

3.6. Geostationary Satellite Data

Geostationary satellites provide imagery for weather forecasting, climate monitoring as well as the early detection of fast developing severe weather. Geostationary satellite data, i.e., precipitation rate, reference evapotranspiration and land surface temperature, that will be used within AFRI4Cast are described in this chapter and are briefly presented in Table 8., as well.

3.6.1. Precipitation rate

Precipitation rate at ground will be derived by the HSAF H03B (P-IN-SEVIRI) product. This product provides rapid precipitation maps derived by IR images from operational satellites which are afterwards tuned by precipiration measurements from passive microwave (PMW) satellite sensors in sun-synchronous orbits.

Specifically, the product H03B (P-IN-SEVIRI Precipitation rate at ground by GEO/IR supported by LEO/MW over the full disk area) is based on the IR images acquired by the SEVIRI instrument on-board Meteosat Second Generation (MSG) satellites (EUMETSAT Satellite Application Facility on Support to Operational Hydrology and Water Management, 2017). The Spinning Enhanced Visible and InfraRed Imager (SEVIRI) is MSG's main instrument being capable of observing the Earth in 12 spectral channels. The spatial coverage of the product encloses the H-SAF area (Europe and Mediterranean basin) along with Africa and Southern Atlantic Ocean, a coverage area that corresponds to 60°S – 67.5°N and 80°W – 80°E. H03B product is generated at the 15-min imaging rate of SEVIRI in the MSG SEVIRI grid at a spatial resolution that changes across the Full Disk varying from 3 km near the sub-satellite point to 8 km on average over Europe.

H03B product is provided in GRIB file format and it can be downloaded using any FTP client through access to ftp://ftphsaf.meteoam.it after a successful registration and login on https://hsaf.meteoam.it. The filename of H03B always specify the product name and its time reference, e.g., h03B_20201201_1415_fdk.grb.gz . Regarding the processing of H03B GRIB files, wgrib2 is a software utility enabling users to convert GRB to TXT file format, while custom Python scripts could be also used for the conversion to TIFF file format.

3.6.2. Reference evapotranspiration

The evapotranspiration rate from a clearly specified reference surface is known as reference evapotranspiration, or Eto. The idea was developed to enable the estimation of the atmospheric evaporative demand regardless of the type of crop, the crop development or the crop management practices. Within AFRI4Cast, reference evapotranspiration will be derived by the DMETREF LSA-303 product.

The Satellite Application Facility (SAF) on Land Surface Analysis (LSA) is part of the SAF Network, a set of specialized development and processing centers, functioning as EUMETSAT distributed Applications Ground Segment (EUMETSAT LSA SAF, 2016). DMETREF LSA-303 product is estimated from the Daily Downward Surface Shortwave Flux (DIDSSF) product generated by the LSA SAF from SEVIRI/Meteosat at an imaging-repeat cycle of 15 minutes and a spatial resolution of 3 km at sub-satellite point.

DMETREF LSA-303 product is available from LSA SAF website http://landsaf.ipma.pt or via an FTP request. This product is distributed in HDF5 file format containing the reference evapotranspiration values as well as the respective quality flags. The files follow the name convention:

HDF5_LSASAF_MSG_METREF_MSG-Disk_ YYYYMMDDHHMM

where YYYY, MM, DD, HH and MM respectively, represent the year, the month, the day, the hour and the minute of for which the product is valid.

3.6.3. Land Surface Temperature

The radiative skin temperature over land is known as the Land Surface Temperature (LST). LST is crucial to understanding land surface physics as it participates in the processes of energy and water exchange with the atmosphere. A wide range of fields related to land surface processes, such as meteorology, hydrology, agrometeorology, climatology, and environmental studies, are particularly interested in accurate LST values.

In the terms of AFRI4Cast, MSG Land Surface Temperature (MLST) values will be used along with LST from other previously mentioned LST data products. Specifically, the product MLST_Dir (LSA-004) comprises a development of the first MLST (LSA-001) product. The MLST_Dir provides LST estimations as retrieved using a Generalised Split-Window (GSW) algorithm and based on MSG/SEVIRI split-window channels R10.8 and IR 12.0 (EUMETSAT LSA SAF, 2022) at an imaging-repeat cycle of 15 minutes and a spatial resolution of 3 km at sub-satellite point.

MLST_Dir (LSA-004) product is available from the LSA-SAF webpage or via an FTP request. This product is distributed in HDF5 format containing the LST values, the directional LST values, the LST error-bar and the corresponding quality flags. The files follow the naming convention:

HDF5_LSASAF_MSG_LST_<Area>_YYYYMMDDHHMM

where <Area>, YYYY, MM, DD, HH and MM respectively, describes the geographical region, the year, the month, the day, the hour and the minute of data acquisition.

Table 8. Geostationary satellite data products to be used within AFRI4Cast.

Data Product	Data Source	Derived Parameters	Update frequency	Spatial resolution
H03B	HSAF	Precipitation rate	15 minutes	3 km near the sub-satellite point to 8km on average over Europe

DMETREF LSA-303	LSA SAF	Reference ET	15 minutes	3 km at sub-satellite point
MLST_Dir (LSA-004)	LSA SAF	Land Surface Temperature	15 minutes	3 km at sub-satellite point

4. From input data to services - EO analysis methods & algorithms

4.1. Introduction

One of AFRI4Cast's main project aspects is to deliver an end to end dataflow procedure that will acquire raw EO data from the remote sensing missions of ECOSTRESS and PRISMA, as well other ancillary sources (Meteorological data from HSAF & LA SAF missions), will process them through an EO Data Fusion component to derive spatial/spatiotemporal enhancements of the primary data sources, as standalone EO data product services, and subsequently import the raw and data fused products into a modeling component to finally derive Crop Monitoring data product services, which would aim to contribute to the policy pillars of Food Safety and Food Security.

This data procedure, obviously has notable structure of 2 levels, Data Fusion and Modeling, and each level has specific constraints and requirements, which could not be met simultaneously. Giving a simple example, the Modeling component will provide services on specific pilot areas with the specified crops of interest, and considering the handy ground truth datasets for the tuning and assessment of the model algorithms, these assumptions constrain the spatial extend requirements for EO data. On the other hand, for the Data Fusion component to deliver notable results, different kind of requirements have to be considered, focusing more on the spatiotemporal consistency of the EO data, the presence/concurrence with external datasets of higher spatial resolution for the ground truth validation of EO product services. Thus, alternative sources of EO data have to be considered as well, as a "plan b" for the project to full-fill its goals in the case where the data requirements of both levels of processing, are not met. On Figure 1. a flowchart describing the dataflow procedure of AFRI4Cast is presented.

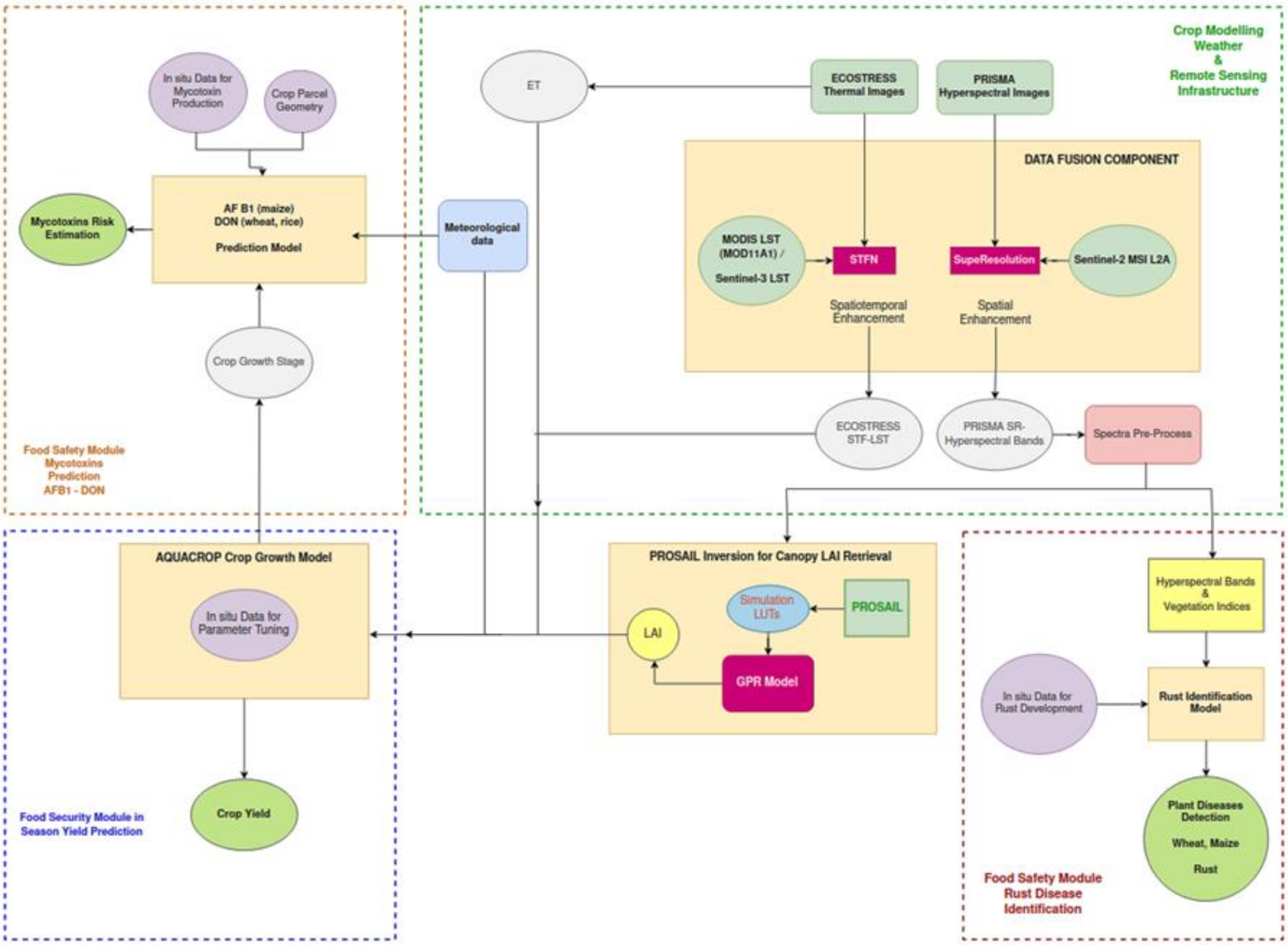

Figure 1. From input data to EO & Crop Monitoring services – AFRI4Cast data processing flow.

4.1.1. EO Data Fusion & Crop monitoring services

In the following tables, the main inputs (Raw Data Products) and outputs (EO & Crop Monitoring Product Services) of the AFRI4Cast project is summarized, as well as some alternative sources for "plan-b" scenarios.

Table 9. Main data inputs, output services and alternative data sources within AFRI4Cast.

Process	Main Source	Alternative Source	Fused with	Service Outputs
Spatial Enhancement	PRISMA	-	Sentinel-2 MSI	PRISMA SR-Hyperspectral Bands/ VIs

Spatiotemporal Enhancement	ECOSTRESS LST	Landsat 8/9 TIRS	MODIS LST *or* Sentinel-3 LST	ECOSTRESS STF-LST

Process	Main Source	Ancillary Source	Alternative Source	Service Outputs
Inversion of PROSAIL RTM	PRISMA SR-Hyperspectral Bands		Sentinel-2 MSI L2A	Canopy Biophysical Parameters – LAI
Crop Growth Modeling – AQUACROP	ECOSTRESS ET – STF-LST	HSAF – LSAF Meteo data	MODIS LST & ET / Sentinel-3 LST	Crop Yield
Aflatoxins Modeling – AF B1 & DON	ECOSTRESS ET – STF-LST	AQUACROP – Crop Growth Stage	MODIS LST & ET or Sentinel-3 LST	Aflatoxin Risk Estimation
Rust Modeling	PRISMA SR-Hyperspectral Bands		Sentinel-2 MSI L2A	Rust Disease Risk Estimation

4.2. EO Data requirements

This chapter targets on describing the requirements that should be determined for the Earth Observation (EO) data in terms of AFRI4Cast. The EO data requirements are divided into minimum and maximum requirements according to the EO data's purpose of use. Minimum requirements refer to the EO data deployed in data fusion techniques and in the spatial or temporal enhancement of hyperspectral and thermal data as well, i.e. PRISMA and ECOSTRESS imagery, respectively. Maximum requirements concern the EO data harnessed for the assimilation of data into crop growth and disease models exploited within AFRI4Cast. Each type of EO data requirements is described in the sections below.

4.2.1. Minimum requirements: For EO Data fusion and enhancement

Thermal imagery

- Short gap between each high spatial resolution thermal acquisition (ECOSTRESS), 4 to 8 days
- Availability of in situ LST data from meteorological stations (Air Temperature or Radiant Temperature/not necessarily over the pilot areas) for the external validation of the Data Fusion product with ground truth of higher resolution
- For the development of an EO Service of data fused products, a constant and consistent data flow from the source API.

Hyperspectral imagery

- Concurrence of hyperspectral imagery with Sentinel-2 imagery
- Concurrence of PRISMA hyperspectral imagery (not necessarily over the pilot areas) with high resolution hyperspectral L2 datasets of BOA reflectance (Historical or current airborne missions, such as AVIRIS or DLR HySpex) for the external validation of the Data Fusion product with ground truth of higher resolution
- For the development of an EO Service of data fused products, a constant and consistent data flow from the source API.

4.2.2. Maximum requirements: For data assimilation into crop growth & disease models

Thermal imagery - Crop Growth Models / Aflatoxin Models

- Spatial coverage and availability over the pilot areas
- Dense LST time series (4 to 8 days ECOSTRESS availability) with day and night acquisitions in order to derive daily minimum and maximum temperature for the AQUACROP model
- Consistent data flow from the source API.

Hyperspectral imagery - Grop growth/ Rust Model

- Spatial coverage and availability over the pilot areas
- Temporal resolution and coverage for a revisit period of 8 - 15 days
- Consistent data flow from the source API.

4.3. Spatial enhancement of PRISMA imagery

4.3.1. Data fusion on Hyperspectral data. A review of state of the art

4.3.1.1. Problem Statement

Hyperspectral sensors offer the opportunity of analyzing the chemical and physical composition of the remotely sensed scene, thanks to their ability of measuring the spectrum of the observed pixels in a large number of contiguous and narrow spectral channels (Yokoya et al., 2017). In particular, space borne sensors allow the exploitation of HS technology for large-scale monitoring of the earth by enabling the identification and discrimination of materials and the derivation of surface parameters at an accuracy level unattainable by currently operational optical broadband (multispectral) satellites.

Taking on account of limitations for imaging cameras, there is the certain trade-off for the spectral resolution and spatial resolution. Hence, HS Imagery with a large number of bands usually has a low spatial resolution to ensure high SNR. On the contrary, imaging sensors can obtain an image with a higher spatial resolution but with a small number of spectral bands, consisting of RGB image, panchromatic image, or multispectral image (MS).

Due to that inevitable trade-off between spatial resolution, spectral resolution, and signal-to-noise ratio (SNR), spaceborne imaging spectrometers are usually designed to provide data with a moderate ground sampling distance (GSD) (e.g., 30 m), limiting the range of potential applications. If higher spatial resolution – possibly multispectral (MS) – data of the scene of interest is available, data fusion can be performed to generate high spatial resolution hyperspectral (HS) data. This data can be thought of as the product of a synthetic sensor featuring the high spatial resolution of the MS sensor and the high-spectral resolution of the HS sensor.

More and more sensors can simultaneously acquire HS and high-resolution MS Imagery on the same scenario, and therefore image fusion approaches can be performed to acquire a fused image with the high spectral resolution and high spatial resolution, which is referred to as HS-MS fusion. This data fusion allows for various new applications potentially conducted on a global scale, which, to data, have been possible only locally with high-spatial-resolution airborne imaging systems. Such applications include high-spatial-resolution ecosystem monitoring, or the high-spatial-resolution mapping of e.g. minerals, urban surface materials, plant species, and many others.

Although the number of available satellite platforms mounting both HS-MS imaging sensors is limited to date , the increasing number and availability of high-resolution optical satellites as well as the ever-improving revisit cycles allow for acquisitions of complementary HS-MS images during the same season and possibly under similar atmospheric and illumination conditions (Chang, 2007).

4.3.1.2. HS-MS Data Fusion Methods

In recent years, several HS–MS fusion approaches have been proposed. They can be grouped into three categories: Pan-sharpening adaptation methods, subspace-based approaches, and Deep Learning algorithms.

Pan Sharpening based HS-MS fusion approaches

Regarding the enhancement of the spatial resolution of MS imagery by fusing the MS data with a corresponding higher-resolution panchromatic image, a large number of pan-sharpening techniques have been developed over the past two decades (Aiazzi et al., 2012).

There are two representative types of pan-sharpening approaches, including Component Substitution (CS) and Multiresolution Analysis (MRA). The CS approaches firstly up-sample the low-resolution MSI as the same spatial size as that of PAN image, and then separate the spatial information and spectral information of up-sampled MSI in distinct components based on specific transformation (intensity hue saturation -IHS, principal-component analysis -PCA, and Gram Schmidt -GS). Subsequently, the spatial information is replaced by the PAN image, and fused MSI is obtained by bringing the replaced spatial information and spectral information back to the image domain via the inverse transformation. In general, CS approaches are easy and can be implemented efficiently. However, they may cause significant spectral distortions because of local dissimilarities between the MSI and PAN image (Vivone et al., 2015).

The MRA methods obtain the fused MSI by injecting the high-resolution structures of the PAN image, which is acquired by a multi-resolution decomposition, into the low-resolution MSI. The approaches in this family differ from using various multi-resolution decomposition method to extract high-resolution spatial structures from the PAN image, with representative ones, the ones comprised of Low-Pass Filtering (Smoothing Filtered based Intensity Modulation – SFIM) and Pyramidal Decompositions (Generalized Laplacian Pyramid –GLP).

Based on recent advances in pan-sharpening, more sophisticated attempts have been made to adapt pan-sharpening techniques to the general HS-MS fusion problem.

Selva et al. (2015) proposed a framework called hypersharpening that effectively adapts MRA-based pan-sharpening methods to HS-MS fusion by synthesizing a high-resolution image for each HS band as a linear combination of MS band images via linear regression. It was shown that the synthesized high-resolution bands used in hypersharpening could lead to significantly better fusion results than a similar yet simpler approach in which for each HS band one high-resolution MS– namely the most correlated – band is selected from the available MS bands rather than synthesized.

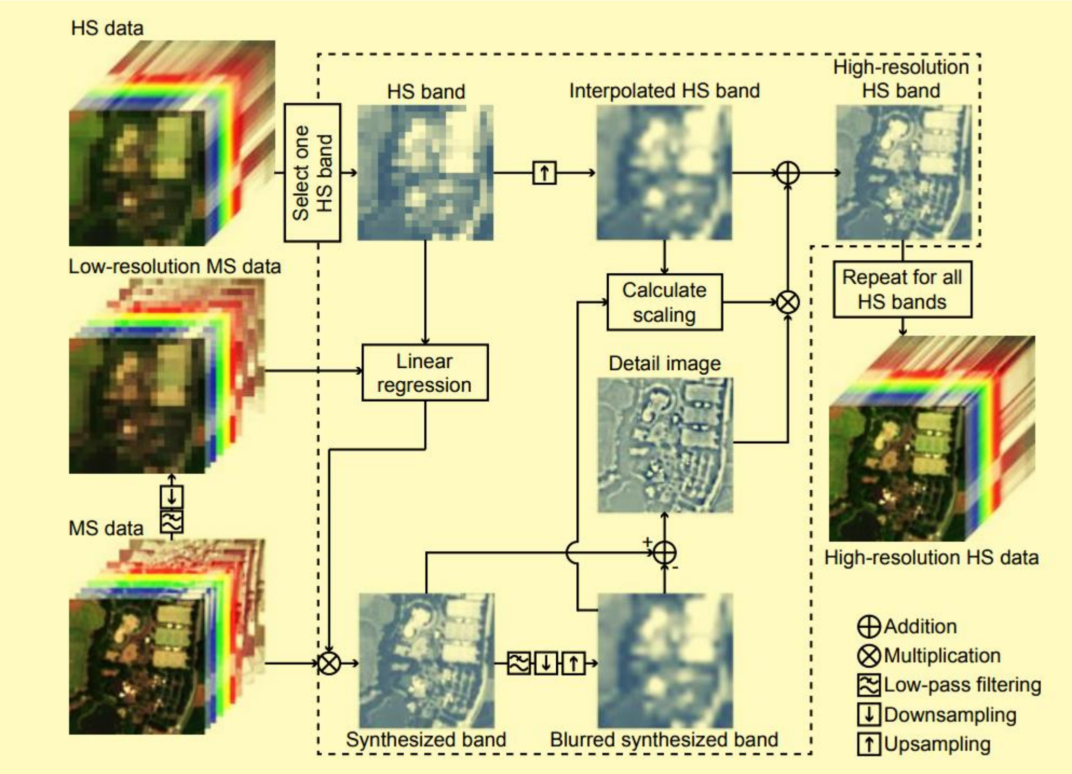

Figure 2. MRA based HS fusion methods (Yokoya N et al. 2017).

According to Yokoya et al. (2017), algorithms that were originally designed for pansharpening and adopted to the HS-MS fusion problem by hypersharpening are well competitive with methods that are specifically developed for HS-MS data fusion. In particular, the methods SFIM-HS and GLP-HS showed stable results above average in the majority of fusion problems, especially when the spectral range of the HS sensor is widely covered by MS bands.

The pan-sharpening based HS – MS fusion methods often have low computation cost and can be implemented fast. They perform reasonably well, however, they often could produce remarkable distortions when the spatial resolutions of HS and MS differ greatly. Moreover, they assume perfect coregistration of the two images, a hypothesis that is difficult to satisfy in practice. In fact, regardless of the adopted coregistration algorithm, residual registration errors still remain that can deteriorate the performance of the HS–MS fusion procedure.

Subspace Methods

Another popular approach fuses the HS-MS images by exploiting the inherent spectral characteristics of the scene via a subspace spanned by a set of basis vectors or spectral signatures of underlying materials (so-called endmembers).

Representing the Bayesian Based methods the MAP algorithm (Eismann and Hardie, 2005) used a stochastic mixing model (SMM) to estimate the underlying spectral scene characteristics and formulates a cost function that optimizes the estimated HS data relative to the input HS-MS images. It should be noted that the optimization of MAPS-MM was processed in the principal component subspace. This idea of fusing the HS-MS images based on spectral information of both input images on a subspace has been the main source of inspiration for many HS-MS fusion methods developed later.

The principles of spectral unmixing have been used in multisensor multiresolution image fusion already around the 2000s. The unmixing-based fusion idea aims at obtaining endmember information and high-resolution abundance matrices from the HS-MS images, respectively, under the constraints of relative sensor characteristics, such as a spectral response function (SRF) and a point spread function (PSF). The fused image can be reconstructed as the product of the two resulting matrices (Delalieux et al., 2014).

The Matrix Factorization based fusion methods intend to estimate the spectral basis and coefficients by solving the corresponding optimization problem. Based on the optimization formulation for the spectral basis and coefficients, the MF based fusion methods mainly has three classes (Yokoya et al., 2011).

The approaches in the first family argue that the spectral information and spatial information mainly relies on the low-resolution HS and high-resolution MS, respectively. Based on this assumption, they estimate the spectral basis only from the observed HS image, and then obtain the coefficients only from the observed MS image.

A second category argues that low-resolution HSI also contains the spatial information and can contribute to the estimation of coefficients. They often firstly compute the spectral basis from observed HSI, and then calculate coefficients from both two images.

The methods in the third category solve the fusion problem based on the coupled matrix decomposition, which is not based on the fixed dictionary, and alternatively update the spectral basis and coefficients. The representative work is coupled nonnegative MF (CNMF). Yokoya et al. (2011) proposed coupled nonnegative matrix factorization (CNMF) that estimates the end member and abundance matrices via alternating spectral unmixing under the constraints of an observation model which incorporates both the relative SRF and PSF.

Although Subspace based approaches have obtained superior performance than the pan-sharpening based methods, they suffer from three disadvantages. First of all, these methods often need to solve the complex optimization problem iteratively, and the computation cost is high. Secondly, the performance of them is usually very sensitive to the parameter selection, and the parameters are hard to set. Finally, they are based on the observation model, and therefore highly rely on accurate estimation of the point spread function (PSF) and spectral response function (SRF).

Deep Learning – Convolutional Neural Networks (CNN)

Recently, Deep Learning CNNs have received more and more attention in many image processing applications due to its high efficiency and promising performance. The CNN is data-driven, and can effectively learn the various image features from the training data (Dian et al., 2021a). Deep Learning CNN based fusion approaches firstly combine the features of the high-resolution MS and low-resolution HS, and then input them into the one-branch CNN to map the high-resolution HS.

In recent years, CNN-based algorithms have also been proposed for the HS–MS fusion problem. Dian et al. (2018) proposed a CNN-based fusion scheme (DHSIS) that exploits both the potential of residual learning and of the Bayesian approach. The method first initializes a high spatial resolution (HR) HS image from the model based fusion framework solving a Sylvester equation. Then, it derives an intermediate HR–HS image exploiting a CNN based on residual learning. This intermediate HR–HS image is returned to the model-based fusion framework to obtain the final super-resolved HS image.

In a representative study, Xie et al. (2019) combined the low-rank constraint of the high-resolution HSI, observation models of the MS and HS, and image prior learned via deep CNN, and formulated the fusion task as a new optimization problem. Based on the proximal gradient method, they designed the deep CNN (MS/HS Fusion Net) to solve the optimization problem in an iterative way.

The CNN based fusion methods are data-driven, often need sufficient HSI and MSI data pairs for the training procedure. However, the training data are often not available. Besides, the generalization ability of these methods is often limited by the imaging models and types of training data. To solve the above problem Dian et al. (2021) introduced a CNN denoiser (CNN – Fus) based HSI-MSI fusion method, which uses the CNN for denoising trained on the gray scaling image. Besides, this method also combines the observation model of the HS and MS into considerations, and it can flexibly deal with different types of data.

There are three advantages of deep CNN based HS-MS fusion methods.

- Firstly, they often do not need to know the PSF and SRF of the sensor, which may be hard to know in practice.
- Secondly, compared with the MF and TR based methods, deep CNN based fusion methods can be implemented much faster, since they do not need iteration and can be easily accelerated via high-performance GPU.
- What is more, the non-linear function and convolution layer can make CNN a powerful ability to learn the image features and achieve robust fusion.

Although the deep CNN based approaches have achieved promising results and high speed for HS-MS fusion, they still have two disadvantages that limit their use in practical remote sensing applications.

Firstly, methods in this family require a large number of images for the training phase, which are often not available. Common practice often lacks the available low-resolution HS, high- resolution-MS, and high-resolution HSI for pre-training. A workout to produce the training data, is regarding the available HS as a reference image, and down-sample it to produce the low-resolution HS and high-resolution MSI, which may not conform to the practical condition (Dian et al., 2021a).

Moreover, the generalization of the deep CNN is also a big challenge. Since the number of spectral bands, spatial resolution, and spectral coverage of the data may be different, CNN trained on one kind of data cannot be applied to the other kinds of data.

4.3.1.3. Challenges on the field of HS – MS data fusion

Hyperspectral Image Fusion has made significant progress in the past ten years. However, significant challenges still remain, which according to Dian et al. (2021b) are regarding :

HS-MS Image Coregistration

The image co-registration intends to geometrically align two images of the same scene acquired by different sensors or at different times. Since HS-MS fusion requires that both images capture the image on the grid system, image registration is a very crucial pre-processing step for the data fusion implementation. The image registration methods are categorized as area-based and feature-based methods. Although image registration approaches, such as scale-invariant Fourier transform, can produce most of the true matches, and there remain some false matches. However, most of the fusion methods assume that the HS and MS are perfectly aligned, and do not account for the distortions caused by the non-rigid registration. The fusion methods, which consider the non-rigid registration, will be a very important topic in future research. Since the deep CNN based methods solve the fusion problem in a supervised way, they may have superiority to reduce the distortions caused by non-rigid alignment.

HS-MS Spatial Resolution difference – spatial downsampling factor

When the spatial resolutions of HS and MS have big differences, the essence of data fusion process is solving a severely ill-posed problem, since most of the spatial information is lost in the hyperspectral acquisition. In this way, the fused HS may contain severe spatial distortions. Therefore, the HSI-MSI fusion for big spatial resolution differences is a very challenging problem, and more efforts need to be made to solve this problem. The key to solving this problem is estimating the spatial degradation model accurately, which can reduce the spatial distortions.

The estimation of PSF and SRF

Many fusion methods, such as Matrix Factorization ones, highly rely on the observation model, which assumes that the PSF and the SRF of the imaging sensor known. In the simulated data fusion experiments, these methods can obtain satisfactory fusion results based on the perfectly-known PSF and SRF. However, they may not produce good fusion results in real data fusion situations, since the PSF and SRF may not be perfectly known in practice, and needs to be estimated in advance.

Computation Efficiency

Since the increased size of HS and MS data availability, the computation efficiency is a very important factor to consider, in the procedure of selecting the appropriate data fusion algorithm. In remote sensing HS-MS fusion, the spatial size is often very large, and the number of spectral bands is usually over one hundred. Hence, the fusion approaches with the low computational cost are highly favored. Most subspace methods suffer from high computational complexities since they need to iteratively solve the complex optimization problem. One available way to reduce the computational cost is low-dimensional subspace representation, which can significantly reduce the size of the spectral mode by exploiting the redundancies in the spectral mode. The other way is towards deep CNN based approaches, which take an end-to-end way to predict the fused HS image without iterative schemes. What is more, they can be dramatically accelerated via the graphics processing unit (GPU) configurations.

Zero-short Learning

The Deep Learning based fusion methods often take an end-to-end approach to learn the mapping from low-resolution HSI and high-resolution MSI to fused HSI. The deep learning based methods can achieve promising performance in terms of quality of fused HSI and computation efficacy. However, methods in this category mainly have two disadvantages when applying them to real data fusion. Firstly, they suffer from insufficient training data. In practice, the training data for HS-MS fusion is often not available. Furthermore, the well-trained deep CNN may have limited generalization ability, since the observational models, spectral range, and the number of spectral bands of the training data and testing data may be different. The possible way to solve the problem is zero-short learning, which trains the deep CNN from the data to be fused. In the training procedure, the training data is generated by spatially downsampling the observed HS and MS, and the observed HS image is used as the output of a deep CNN. In this way, the spatial downsampling procedure for generating training data makes a difference, and the way of spatially downsampling procedure should be learned according to the spatial degeneration between the observed HS and MS.

4.3.2. Data fusion of PRISMA Hyperspectral with S2 Multispectral Images

In the course of the AFRI4Cast project, a major part of the EO data enhancement component will deal with the upgrading of the PRISMA hyperspectral images to a higher spatial resolution. PRISMA satellite payload includes a pushbroom HS camera operating in the visible, near infrared (VNIR) and shortwave infrared (SWIR) spectral ranges. Specifically, the HS imaging sensor covers the portion of the electromagnetic spectrum ranging from 400 to 2500 nm with 10 nm spectral sampling through two partially overlapped spectrometers. Similar to other HS satellite missions the PRISMA HS sensor has a limited spatial resolution because of the limited amount of incident energy. Specifically, its groundsampling distance (GSD) is of 30 m. The aim of PRISMA spatial enchancement is to make the HS data applicable for providing vegetation indices and canopy biophysical parameters and crop disease modeling at a parcel level spatial scale.

A natural solution to enhance the spatial resolution of a satellite HS image is to fuse it with a higher resolution multispectral (MS) image of the same scene, possibly acquired under the same conditions. However, PRISMA mission payload does not include a high spatial resolution MS sensor. Therefore, the only way to apply the HS–MS fusion paradigm to PRISMA data is to exploit the high-resolution MS image provided by other satellite missions. In this context, a great opportunity is offered by the Sentinel-2 (S2) program. Specifically, the Sentinel 2 multispectral bands with spatial resolution of 10 m (B2–B4 and B8) and 20 m (B5–B7, B8a, and B11–B12) cover a spectral range which is overlapped with that of the PRISMA sensor and can be exploited to enhance the spatial resolution of PRISMA data according to theHS–MS fusion framework (Acito et al., 2022).

The PRISMA product to be used will be Level L2D, providing at-surface orthorectified reflectance with additional information of:

- Aerosol Characterization Product
- Water Vapour Map Product
- Cloud Characterization.

The geolocation correction will be carried out by using a Python package based on AROSICS algorithm.
The proposed PRISMA spatial enhancement strategy consists of 3 main steps as shown in the following flowchart.

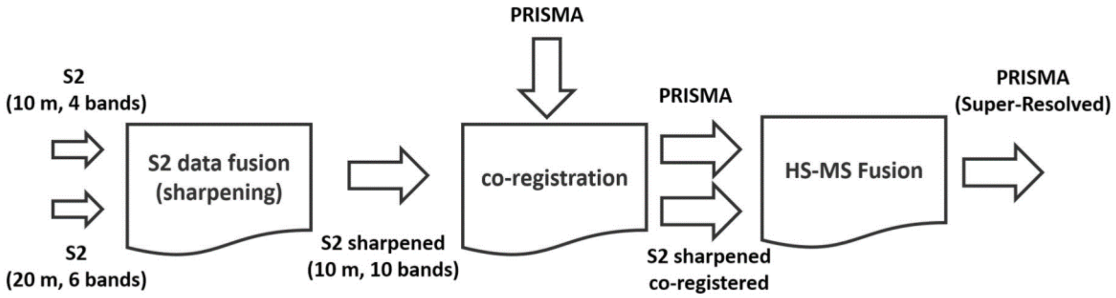

Figure 3. PRISMA - Sentinel 2 Data Fusion general framework (Acito et al., 2022).

S2 Data Fusion

The first step (named S2 data fusion) applies a fusion algorithm to the 10 and 20 m S2 images to obtain a 10 band MS image with the highest spatial resolution which will be used to bring the spatial resolution of the PRISMA image to 10 m. As to the S2 data fusion, the HP adaptation of the MTF–Gaussian Laplacian Pyramid (GLP)–context-based decision (CBD) algorithm proposed in Acito et al. (2022) will be considered. MTF–GLP–CBD is a pansharpening algorithm belonging to the MRA class here chosen because of its computational efficiency and of the good fusion performance experienced on real S2 data.

Coregistration of S2 and PRISMA Images

The second step (coregistration) applies a registration procedure to the MS image resulting from the previous step and the PRISMA image. This step is necessary even in the case of geolocated data to compensate for the inaccuracy of pixel-level coordinates due to errors in the georeferencing process. Image coregistration will be performed assuming an affine transformation between the images and exploiting control points (Cps) detected in an unsupervised manner by the speeded-up robust feature algorithm (SURF).

In general, feature-based techniques start from the extraction of interest points (IPs) independently from the two images to be coregistered named test image and reference image. To each IP, a feature vector is then assigned by exploring the characteristics of the image in a local neighborhood. In our case, the SURF algorithm (Acito et al., 2022) is adopted to extract descriptors that are invariant to scale, rotation, and illumination. IPs from the two different images are tested to find pairwise correspondence between their descriptors. Pairs of IPs with the most similar descriptors are retained and represent the so-called CPs. Finally, the pixel coordinates of each CP in the two images are used to estimate, in accordance with a given model, the transformation that represents the geometrical distortion between the test and the reference image. Once the transformation is estimated, it is applied to resample the test image into the coordinate system of the reference image. The SURF-based procedure summarized above will independently be applied to each band of the two images, Fused S2 and PRISMA. The CPs extracted in all the bands will be merged together and used to estimate the geometrical distortion assuming an affine transformation with a scale ratio of 3, according to the GSDs of the two considered images.

Hyperspectral -Multispectral Data Fusion

The third step finally applies a HS–MS pansharpening fusion approach to obtain a super-resolved PRISMA image. HS–MS fusion is surely the most critical step of the PRISMA spatial enhancement scheme. Several algorithms have been proposed in the past years, as summarized in the abovementioned review chapter. Most of them assume perfect coregistration of the two images, a hypothesis that is difficult to satisfy in practice. Regardless of the adopted coregistration algorithm, residual registration errors still remain that can deteriorate the performance of the HS–MS fusion procedure. For this reason, we propose two modified versions of the well-known smoothing filtered-based intensity modulation (SFIM) algorithm specifically designed to be robust to residual registration errors, as our main HS–MS fusion scheme. The hyperspectral adaptation of the SFIM algorithm called SFIM-HP. It sharpens the low spatial resolution image by multiplying the upsampled lower resolution image by the ratio between the higher resolution image and its low-pass filtered version on a pixel-by-pixel basis. Of course, the main assumption/precondition is that PRISMA and S2 images must be acquired on the same scene and with the minimum time difference in order to limit the potential seasonal changes in the monitored surface.

In general Acito et al. (2022), SFIM-HP introduces relatively small spectral distortions on the super-resolved image. Conversely, it is sensitive to coregistration errors. In addition, it also requires knowledge of the parameter c which may not be available in real applications. Notice that, despite the efforts made to choose the best algorithm to geometrically align the two images, residual coregistration errors will always occur in practice and should be properly considered in the fusion strategy. The previous considerations suggest the use of modified versions of SFIM-HP that are more robust to residual registration errors and do not require the knowledge of c. Such robust versions of SFIM-HP will be referred to as RSFIM-HP. Acito et al. (2022), suggest two modifications on the implementation strategy of RSFIM-HP, named soft and hard respectively.

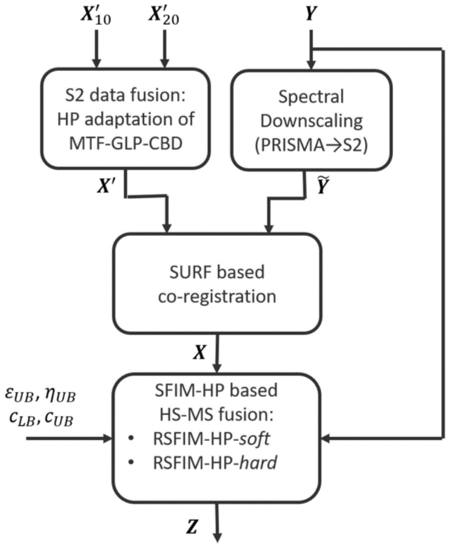

Figure 4. PRISMA (Y) - Sentinel 2 (X) data fusion for Spatial Enhancement (Acito et al., 2022).

The hard strategy represents the natural choice in absence of noise in the data. In the presence of noise, which in each pixel can be realistically modeled as a spectrally uncorrelated zero mean random vector, the hard strategy tends to bring the noise components of the HS image in the super-resolved image. To mitigate noise effects, the soft strategy is proposed where the weighting coefficients are defined so as to assign greater weights to solutions more consistent with the higher spatial resolution image. RSFIM-HP-soft is expected to be more robust to noise thanks to the filtering effect introduced by the weighted sum. This is particularly true in the homogeneous regions of the scene where the weights are very similar. Conversely, it is expected to introduce a smoothing effect on sharp variations thus performing worse than RSIM-HP-hard in preserving edges.

This main HS data fusion scheme of RSFIM-HR will be compared – benchmarked to a Deep Learning CNN approach, to test the effectiveness of the fusion result, on a “real” remote sensing dataset. A residual network (ResNet) is formed by stacking several residual blocks together. Each residual block consists of convolution layers, batch normalization, and activation layers. The batch normalization processes the data and brings numerical stability by using some scaling techniques without distorting the structure of the data. The activation layer is added into the residual network to help the neural network to learn more complex data. The CNN or deep learning method uses ReLU (rectified linear unit) function in the activation layer to accommodate the nonlinearity nature of the image data while providing the output. The residual blocks allows information to flow from the first layer to the last layers of the network by adding residual or skip connection strategies. Therefore, ResNet can effectively utilize features of the input data to the output of the network and thus alleviate gradient vanishing problems (Priya and Rajkumar, 2022).

The ResNet fusion architecture for HS–MS fusion, as presented by Priya and Rajkumar (2022) uses residual or skip connection which helps to improve the feature extraction capability from the images. For implementation, a 1D ResNet will be used to extract the spectral features from the PRISMA image (Spectral generative network) and 2D ResNet for extracting spatial features from S2 Fused Image (Spatial generative network). Both 1D and 2D ResNet architecture consist of three residual blocks each having two convolutional layers and 64 filters.

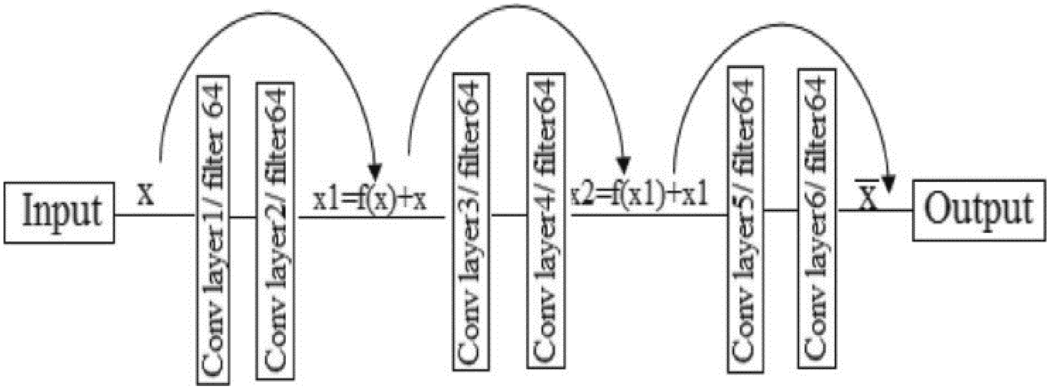

Figure 5. Residual block with two stacked layer (Priya and Rajkumar, 2022).

A 3X3 kernel size for 2D Resnet and 1X3 kernel size for 1D Resnet will be used for extracting the spatial and spectral data from MSI and HSI. Each residual block will employ a ReLU activation layer to accommodate the nonlinearity constraints included in the proposed hyperspectral image fusion model. Finally, the feature embedding and image reconstruction process are performed using another 2D CNN. The spectral information from PRISMA and spatial data from Fused S2 will finally be extracted using ResNet by element-wise multiplication. The architecture of the ResNet model is shown on Table 10.

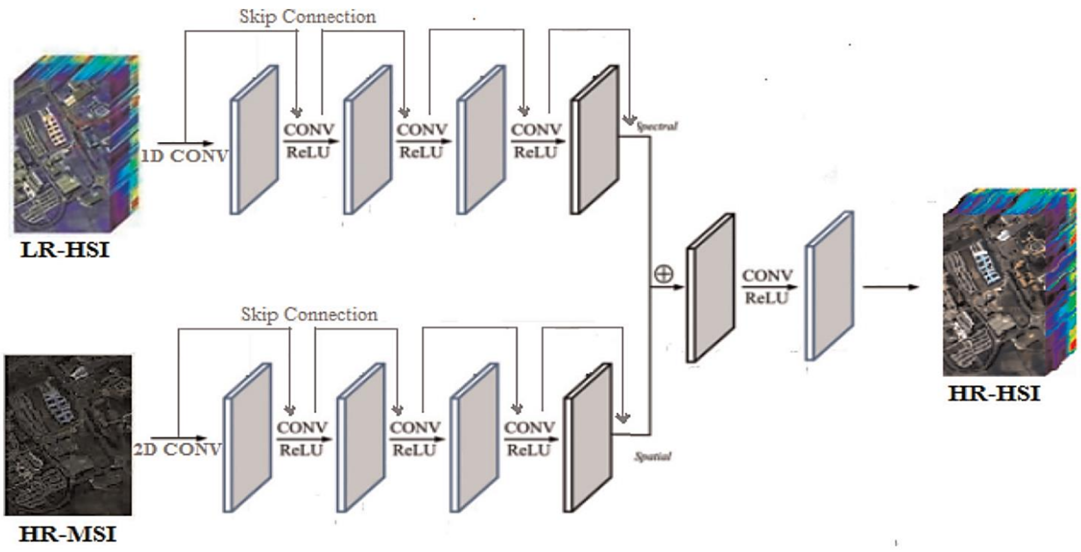

Figure 6. The framework of the proposed ResNet Fusion architecture (Priya and Rajkumar, 2022).

The evaluation aspects of the Hyperspectral Data fusion products and the relevant validation methodology will be presented on the AFRI4Cast deliverable D6.

4.3.3. Service outputs

The PRISMA spatial enhancement component will use the proposed methodology in order to deliver to AFRI4Cast the following product services:

Hyperspectral Bands: Image layers in a continuum of 239 spectral bands ranging from 400 to 2500 nm, 66 in the VIS-NIR, and 173 in the SWIR spectrum, with a spectral resolution smaller than 12 nm and a spatial resolution of 10 m GSD.

Vegetation Indices: The Rust disease assessment will be accomplished with the aid of narrowband Vegetation Feature Indices needed to monitor the crop status and detect the presence of diseases or pests which could affect the crop nutrition quality and yield. AFRI4Cast will regard the following Vegetation Indices:

- Normalized Difference Vegetation Index, NDVI = (R830−R675)/(R830+R675)
- Structural Independent Pigment Index, SIPI = (R800−R445)/(R800−R680)
- Photochemical Reflectance Index, PRI = (R570–R531)/(R570+R531)
- Plant Senescence Reflectance Index, PSRI = (R680−R500)/R750
- Modified Simple Ratio, MSR = (R800/R670−1)/sqrt(R800/R670+1)

All Vegetation Indices will be provided at a 10 m spatial resolution.

Table 10. Architecture of the ResNet model.

Name	Layer	Kernel Size	Input Size	Input Content	Stride	Padding	Activation	Output Size	Output Content
Input Layer	Conv 1	ID-CNN 1*3	1	1D Image(Spectral)	1	same	ReLU	64	1DConv1
		2D-CNN 3*3	2	2D Image(Spatial)	1	same	ReLU	64	2DConv1
Residual Block1	Conv 2	1D-CNN 1*3	64	1DConv1	1	same	ReLU	64	1DConv2
		2D-CNN 3*3	64	2DConv1	1	same	ReLU	64	2DConv2
	Conv 3	1D-CNN 1*3	64	1DConv2	1	same	ReLU	64	1DConv3
		2D-CNN 3*3	64	2DConv2	1	same	ReLU	64	2DConv3
Skip Connection	Add 1			1DConv1 + 1DConv3					1DResB1

				2DConv1+ 2DConv3					2DResB1
Residual Block2	Conv 4	1D-CNN 1*3	64	1DResB1	1	same	ReLU	64	1DConv4
		2D-CNN 3*3	64	2DResB1	1	same	ReLU	64	2DConv4
	Conv 5	1D-CNN 1*3	64	1DConv4	1	same	ReLU	64	1DConv5
		2D-CNN 3*3	64	2DConv4	1	same	ReLU	64	2DConv5
Skip Connection	Add 2			1DConv1 + 1DResB1 + 1DConv5					1DResB2
				2DConvt1 + 2DResB1 + 2DConv5					2DResB2
Residual Block3	Conv 6	1D-CNN 1*3	64	1DResB2	1	same	ReLU	64	1DConv6

		2D-CNN 3*3	64	2DResB2	1	same	ReLU	64	2DConv6
	Conv 7	1D-CNN 1*3	64	1DConv6	1	same	ReLU	64	1DConv7
		2D-CNN 3*3	64	2DConv6	1	same	ReLU	64	2DConv7
Skip Connection	Add 3			1DConv1 + 1DResB1 + 1DResB2 + 1DConv7					1DResB3
				2DConv1 + 2DResB1 + 2DResB2 + 2DConv7					2DResB3
Max pooling	Conv 8	1D-CNN 1*3	64	1DResB3	1	same	ReLU	64	1DConv8
		2D-CNN 3*3	64	2DResB3	1	same	ReLU	64	2DConv8
Flatten layer	Conv 9	1D-CNN 1*3	32	1DConv8	1	same	ReLU	1	Spectral data

		2D-CNN 3*3	32	2DConv8	1	same	ReLU	1	Spatial data
Upsampling layer	Conv 10	2D-CNN 3*3	1	Spectral/Spatial data	1	same	ReLU	32	Spectral*Spatial
Output layer	Conv 11	2D-CNN 3*3	32	Spectral * Spatial	1	same	ReLU	64	Fused Image

4.4. Canopy Biophysical parameters estimation from hyperspectral remote sensing

Biophysical parameter retrieval is an approach in remote sensing that aims to estimate parameters which have physical meaning related to properties of living organisms. The goal is to provide values directly relating to the biophysical state, but independent of acquisition conditions and technology. Important parameters describing canopy structure include leaf area index (LAI), green cover fraction (fCover), fraction of absorbed photosynthetically active radiation (fAPAR), canopy chlorophyll content (CCC), canopy water content (CWC), etc.. These canopy biophysical parameters are synthetically defined as (S2ToolBox Level 2 products, 2020):

- LAI is defined as half the developed area of photosynthetically active elements of the vegetation per unit horizontal ground area. This is an intrinsic canopy primary variable that should not depend on observation conditions. LAI is strongly nonlinearly related to reflectance.
- FAPAR corresponds to the fraction of photosynthetically active radiation absorbed by the canopy. It depends on canopy structure, vegetation element optical properties and illumination conditions. FAPAR is relatively linearly related to reflectance values, and will be little sensitive to scaling issues.
- FVC is used to separate vegetation and soil in energy balance processes, including temperature and evapotranspiration. It is computed from the leaf area index and other canopy structural variables and does not depend on variables such as the geometry of illumination as compared to FAPAR. Because of its quasi-linear relationship with reflectances, FVC will be only marginally scale dependent.
- CCC is a very good indicator of stresses including nitrogen deficiencies. It is strongly related to leaf nitrogen content (Houlès et al., 2007). This quantity can be calculated both at the leaf level and at the canopy level by multiplication of the leaf level chlorophyll content by the leaf area index. Studies have demonstrated that a direct estimation of CCC is more robust and accurate than an estimation based on the product of the individual estimation of LAI and C_{ab} (Weiss et al., 2004).
- CWC is proposed as a possible candidate to estimate water present in a plant. Water represents between 60 % and 80% of the living plant mass. Since radiation is absorbed significantly by water in the near and middle infrared, the spectral configuration of Sentinel-2 allows accessing this variable.

Methods to retrieve these parameters from remote sensing data fall into two main categories. Statistical models empirically match data to a biophysical variable. Univariate techniques use a single quantity derived from the data, usually a vegetation index whereas multivariate techniques link a combination of measurements at different wavelengths to one or more biophysical parameters. Physically based modeling is an alternative approach which uses advanced radiative transfer models to describe the transfer and interaction of radiation inside a leaf or canopy based on robust physical, chemical, and biological processes. They compute the interaction between solar radiation and plants and provide as such a better understanding between biophysical variables and reflectance characteristics. The PROSAIL model, a fusion of PROSPECT (leaf reflectance and transmittance) and SAIL (plant canopy reflectance), has been used for the last thirty years to simulate the spectral and directional reflectance of plant canopies in the solar domain. It links the spectral dimension of the reflectance, which is mainly related to the biochemical content of the leaves, to the directional dimension, which is mainly related to the architecture of the canopy. PROSAIL has been widely used to develop new methods to retrieve biophysical properties of vegetation and to prepare new space missions. Applications are numerous in agriculture, forestry, ecology, climatology, exobiology, etc. Because of its ease of use, robustness and regular updates, PROSAIL has become one of the most popular tools for radiative transfer in vegetation. PROSAIL model and our approach to estimate LAI parameter from PRISMA and/or Sentinel-2 images will be described in the following paragraphs.

Regarding the statistical models, hyperspectral sensors allow to compute many spectral indices capable to highlight specific traits of the vegetation. A list of them with the corresponding formulas are described in Appendix 1.

Physically based methods were shown to be more robust, accurate, and transferable over various cover types and environments (Kganyago et al., 2021). However, physically based approaches are ill-posed (i.e., different combinations of canopy parameters may correspond to almost similar spectra, thus yielding inconsistent results), complex, and computationally expensive. This is much true if the objective is the development of a model capable to exploit hyperspectral data. In contrast, nonparametric approaches, i.e., MLRAs (Machine Learning Regression Algorithm), are relatively fast, and can learn non-linear relationships. Recent studies show that the coupling of physically based approaches and MLRAs, yields better prediction accuracies. These approaches are available operationally, such as the Sentinel-2 Level-2 Prototype Processor (SL2P) implemented in the Sentinel Application Platform (SNAP) for Sentinel-2 MSI. Taking into account the results of some validation and intercomparison studies (Bochenek et al., 2017; Brown et al., 2021; Kganyago et al., 2020) a specific ML approach is developed for the areas of interest, the crops under study and the characteristics of the satellite sensors we aim to exploit.

4.4.1. PROSAIL Model description

RTM-inversion (Radiative Transfer Model) methods have the advantage of a physical foundation that allows their application on a global scale (Yebra et al., 2013) and the knowledge of the satellite observation angles allows their inclusion in the inversion method. In optical remote sensing of vegetation, RTMs are used to model the phenomena of light interception by plant canopies and to interpret vegetation reflectance in terms of biophysical characteristics (Jacquemod et al., 2009). They have been widely used to design and exploit vegetation indices and to develop inversion procedures to estimate vegetation parameters from remotely sensed data. The PROSPECT leaf optical properties and the Scattering by Arbitrarily Inclined Leaves (SAIL) canopy bidirectional reflectance model are still the most popular and accurate (Jacquemod et al., 2000). In the nineties, these models have been coupled into PROSAIL, which allows to model both the spectral and the directional variation of canopy reflectance as a function of leaf biochemical properties such us chlorophyll content, water content, pigment concentration on the leaf side, and in terms of Leaf Area Index (LAI), leaf orientation on the canopy side. Furthermore, in 2001 SAIL was coupled with the Jasinski geometric model (Jasinski et al., 1989). to create GeoSail (Huemmrich, 2001), allowing to properly describe radiation reflected by discontinuous vegetation. The PROSPECT and SAIL models are coupled so that the simulated leaf reflectance and transmittance from PROSPECT are fed into the SAIL model, completed with information about soil optical properties and illumination/observation geometry (Fig. 7).

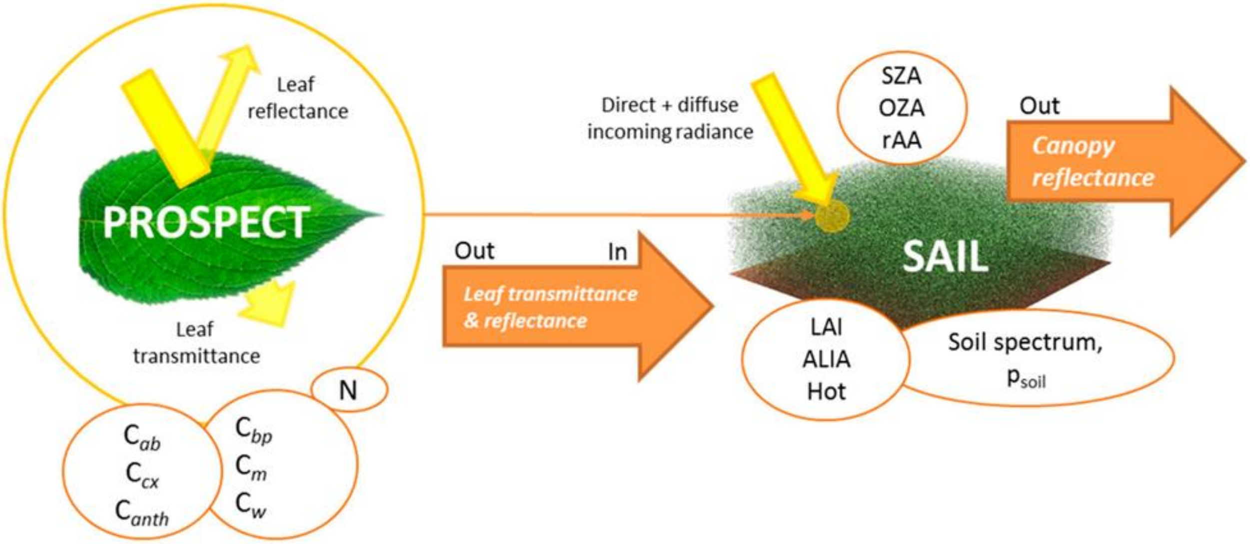

Figure 7. Calculation of canopy reflectance using the coupled PROSPECT + SAIL models. Variable symbols are explained in Table 11 and in the text.

Table 11. Overview of the input parameters of the PROSAIL model with symbols, units and typical variable ranges published in the literature for five different crops that have been analyzed most often by the studies.

Parameter	Symbol	Units	Typical Ranges for Crops		
			Maize [1, 2, 3]	**Wheat [3, 4]**	**Rice [5, 6]**
Leaf Model: (PROSPECT-D)					
Leaf structure index	N	Unit less	1.2–1.8	1.0–2.5	1.0–2.0
Chlorophyll a + b content	C_{ab}	$(\mu g/cm^2)$	0–80	0–80	0–80
Total carotenoid content	C_{cx}	$(\mu g/cm^2)$	1–24	1–24	4–17
Total anthocyanin content	C_{anth}	$(\mu g/cm^2)$	-	-	-
Brown pigments	C_{bp}	Unit less	0–1	0–1	0–1
Dry matter content, or leaf mass per area	C_m/LMA	(g/cm^2)	0.004–0.0075	0.001–0.02	0.001–0.02
Equivalent water thickness, or water depth	EWT/C_w	(cm)	0.01–0.03	0.001–0.05	0.001–0.002
Canopy Model: (4SAIL)					

Parameter	Symbol	Units	Typical Ranges for Crops		
			Maize [1, 2, 3]	**Wheat [3, 4]**	**Rice [5, 6]**
Leaf area index	LAI	(m^2/m^2)	0–7	0–8	0–10
Average leaf inclination angle * or: Leaf inclination distribution function **	ALIA $LIDF_{a/b}$	(°) (°)	20–70	20–90	20–80
Hot spot parameter	Hot	(m/m)	0.01–0.2	0.01–0.5	0.01–0.1
Soil reflectance	ρ_{soil}	(%)			
Soil brightness factor	α_{soil}	Unit less	0.5–1.5 *** or 0–1 ****		
Fraction of diffuse illumination	skyl	Unit less	23% for a standard clear sky		
Sun zenith angle	SZA/θ_s	(°)	According to actual conditions during data/image acquisition		
Viewing (observer) zenith angle	OZA/θ_v	(°)			
Relative azimuth angle between sun and sensor	rAA/$ø_{SV}$	(°)			

* characterizes an ellipsoidal leaf inclination model; ** spherical, planophile, erectophile, uniform, extremophile or plagiophile types. LIDF is characterized by LIDFa, which controls the average leaf slope and LIDFb which controls the distribution's bimodality; *** to be multiplied with single ρsoil spectrum; **** scaling factor between the two model-implemented ρsoil spectra (wet versus dry).

The leaf optical properties model PROSPECT is central to the success of PROSAIL as it simulates the spectral range from 400 to 2500 nm with only a limited number of parameters, describing the biophysical properties of a single leaf. PROSPECT as received several modifications. Most recent versions include, a part the leaf mesophyll (N), chlorophyll a + b concentration (C_{ab}), and leaf water content (C_w), other parameters, such as dry matter content (C_m) or leaf mass per area (LMA), brown pigments (C_{bp}), and total carotenoid content (C_{cx}). In the newest version "PROSPECT-D", besides a new calibration of specific absorption coefficients (SAC) of each pigment, leaf anthocyanin content (C_{anth}) was added.

The SAIL radiative transfer model is based on the 1-D model developed by Suits to simulate bidirectional reflectance of a canopy. PROSAIL also permits to calculate the fraction of absorbed photosynthetically active radiation (fAPAR), and the fraction of vegetation cover (fCover). The SAIL model represents the canopy structure in a simple way and requires only a few parameters. These include leaf reflectance and transmittance (obtained from the PROSPECT output), leaf area index (LAI), and leaf inclination distribution function (LIDF). Additionally, information about viewing geometries, i.e., sun and sensor (observer) zenith angles (SZA and OZA, respectively) as well as the relative azimuth angle between both (r_{AA}), must be provided by the user. The fraction of diffuse incident solar radiation (skyl) is another input into the model. Moreover, a soil reflectance factor (α_{soil}) is used to mimic moisture-induced reflectance changes of the upper soil layer (ρ_{soil}).

Summarizing, the current PROSAIL model calculates the canopy bidirectional reflectance from 400 to 2500 nm in 1 nm increments as a function of up to 16 input parameters, defining pigment and water content, canopy architecture, soil background, hot spot, solar diffusivity, as well as observation geometry. All parameters of the PROSPECT and SAIL model family are listed in Table 11, including their symbols and units. Additionally, crop-specific parameter ranges are listed for crops of interest in AFRI4Cast: maize, wheat, rice. Note that these ranges rely purely on values found in the literature and may underlie changes.

PROSAIL has been used in forward mode, i.e., calculation of canopy reflectance using different input parameters, for diverse purposes. For example, a common objective of studies using the model in forward mode was to examine the sensitivity of bi-directional canopy reflectance to different factors, for instance the effect of parameters on the red edge position (REP) of vegetation. Other studies evaluated the sensitivity of canopy reflectance to leaf optical properties. In this way, researchers found for example that the sensitivity of canopy reflectance to leaf reflectance is significant for large vegetation cover fractions only in spectral domains with low absorption. Also, the influence of the observation geometry on red and near infrared (NIR) reflectance was investigated. Other factors, such as sensitivity to canopy architecture, soil background reflectance, and atmospheric conditions were examined. The PROSAIL model was also exploited for the design of new (improved) vegetation indices.

A scheme of as PROSPECT and SAIL are coupled is given in Fig. 8.

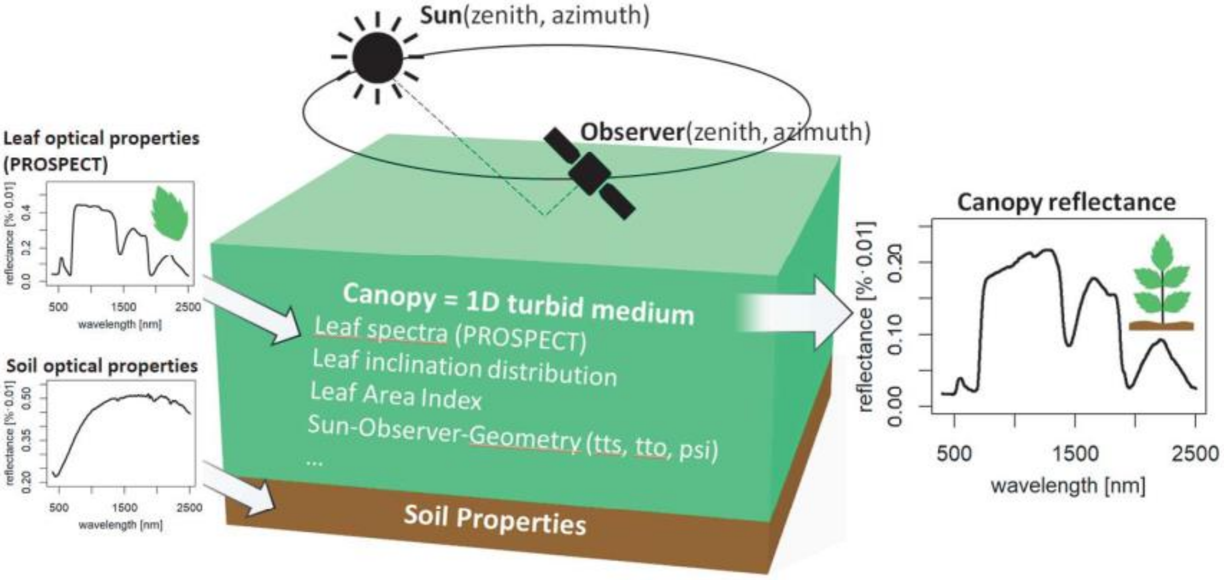

Figure 8. PROSPECT + SAIL coupling scheme (Kattenborn, 2019): PROSPECT uses a description of the leaf in terms of its structure (N) and biochemical composition (Cab, Canth, Cw, …) to output the leaf transmittance and reflectance. These values are used by SAIL to build the canopy model in conjunction with the leaf inclination and density (LIDF, LAI) and a soil spectrum (ρsoil, psoil). The solar illumination parameters (SZA, SAA) and the viewing angles (VZA, VAA) allow to determine the canopy reflectance that reaches the viewer.

4.4.2. Review on PROSAIL Inversion methods for the retrieval of LAI parameter - Application on AFRI4Cast

RTM Inversion Strategy

Our vegetation modelling strategy is based on (Danner et al., 2021) and (Pampanoni et al., 2022), which can be considered the state of the art regarding LUT-based approach and ML inversion for LAI from satellite images, based on the PROSAIL-adjacent RTMs. The combination of PROSPECT-D and 4SAIL is used to model croplands, which are assumed to be homogeneous vegetated pixels. To model the cropland understory we will combine the *pyprosail* package dry and wet soil spectra in different proportions using the psoil parameter.

The RTM inversion strategy applied to these two model combinations is based on the use of LUTs, again similarly as (Danner et al., 2021). Before describing the methodology adopted to create and invert the LUTs, we will perform a sensitivity analysis of the two model combinations in order to verify that the model is sensitive to the variables that allow us to calculate the LAI, and in particular to identify the ideal Sentinel-2 and PRISMA channels to use to successfully perform the inversion.

Sensitivity Analysis of the Combined Models

Before attempting to retrieve the biophysical parameters from satellite observations using a model inversion technique, it is mandatory to verify the feasibility of the retrieval on a variable-by-variable basis. If a variable does not have any significant effect on the variation of the model output, it will be very difficult to invert it, because the model will barely react even to large variations of the variable. To this end, we will use Global Sensitivity Analysis (GSA) (Sobol, 2001, 1993), often used to quantify the effect of the uncertainty on a variable on the uncertainty of the model output (Saltelli, 2002). In particular, the Sobol method allows to obtain both first-order sensitivity indices, which quantify the contribution of each variable per se, i.e. while all the other variables are kept constant, and higher-order sensitivity indices that account for the interactions between variables. The possibility to take into account the interactions between variables is fundamental, because some variables that may appear to be not significant at the first-order, may become significant through interactions. The total-order sensitivity index of the i-th variable is the sum of the first-order sensitivity index of that variable and of all the higher-order sensitivity indices associated to its interactions with the other variables. These calculations will be carried out using the SALib Python library (Herman and Usher, 2017), which makes it straightforward to construct the necessary sequences for each model parameter through the Saltelli module, requiring only the definition of the variation interval of each variable as an input. The module returns quasi-random, low-discrepancy sequences calculated in order to sample the parameter space as uniformly as possible by exploiting Saltelli’s sampling scheme, which is an improvement of Sobol’s (Herman and Usher, 2017). The sequences are then used as inputs for the pyprosail Python library, and the resulting outputs are ran through the sobol.analyze function which performs the Sobol Global Sensitivity Analysis returning both first-order indices and total-order indices.

Table 12. Example of Parameter bounds used for the GSA of the combination of PROSPECT-D and 4SAIL.

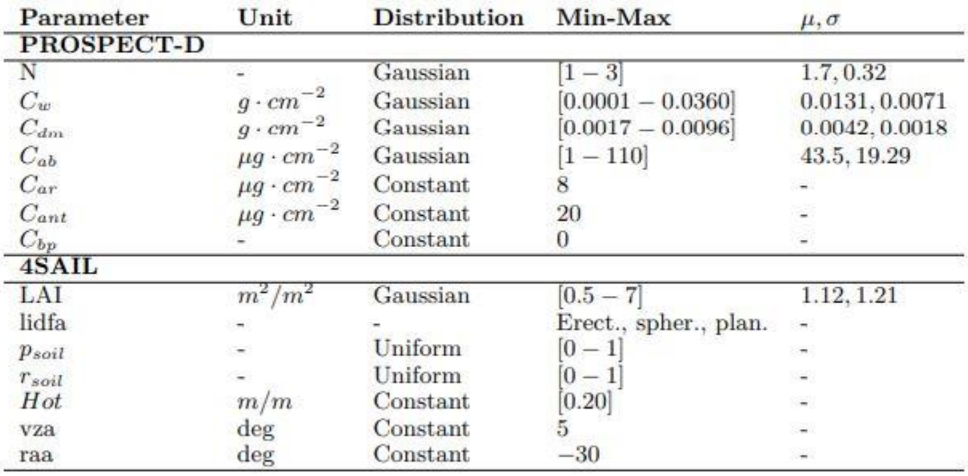

Parameter	Unit	Distribution	Min-Max	μ, σ
PROSPECT-D				
N	-	Gaussian	$[1-3]$	$1.7, 0.32$
C_w	$g \cdot cm^{-2}$	Gaussian	$[0.0001-0.0360]$	$0.0131, 0.0071$
C_{dm}	$g \cdot cm^{-2}$	Gaussian	$[0.0017-0.0096]$	$0.0042, 0.0018$
C_{ab}	$\mu g \cdot cm^{-2}$	Gaussian	$[1-110]$	$43.5, 19.29$
C_{ar}	$\mu g \cdot cm^{-2}$	Constant	8	-
C_{ant}	$\mu g \cdot cm^{-2}$	Constant	20	-
C_{bp}	-	Constant	0	-
4SAIL				
LAI	m^2/m^2	Gaussian	$[0.5-7]$	$1.12, 1.21$
lidfa	-	-	Erect., spher., plan.	-
p_{soil}	-	Uniform	$[0-1]$	-
r_{soil}	-	Uniform	$[0-1]$	-
Hot	m/m	Constant	$[0.20]$	-
vza	deg	Constant	5	-
raa	deg	Constant	-30	-

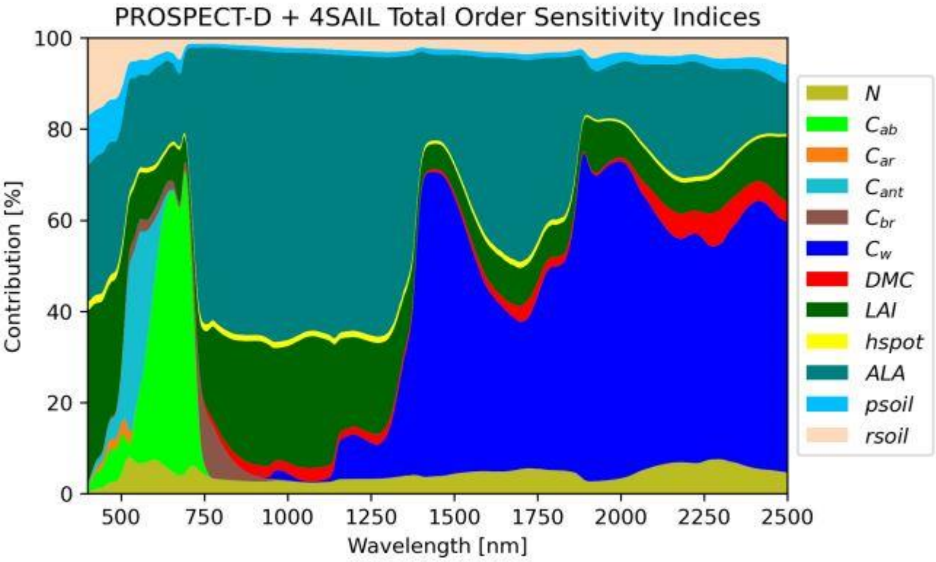

Figure 9. Example of GSA of the PROSPECT-D + 4SAIL radiative transfer models. The stacked plot shows the progression of the total order sensitivity indices of each parameter of the combined model in the portion of the spectrum supported by PROSPECT. Viewing angles have not been included in the GSA, since their value is always known. This figure was taken from (Pampanoni et al., 2022).

LUT-based Inversion

The core idea is based on a coupling scheme of PROSAIL as a well-known RTM with fast and an efficient machine learning regression algorithm.

Generation of the LUTs

To generate the LUT, the PROSAIL model was run in forward mode to simulate canopy reflectance for an appropriate number of parameter combinations. the LUT calculation process takes place as follows:

- Definition of the LUT target size: we tested LUT sizes ranging from 10000 to 200000 samples. A LUT size of 100,000 parameter combinations was found to achieve a good compromise between the computer resource requirement and the accuracy of canopy variable estimation (Weiss et al., 2004). The 100,000 parameter combinations were randomly generated with uniform or normal distributions and specific ranges for the variables.
- Definition of the LAI minimum and maximum values.
- Creation of first-guess distributions for each variable: after setting a seed for the random number generator, we independently create distributions of values for each model parameters.
- Elimination of unlikely combinations
- Sample selection: once we have an adequate number of samples, in order to match the LUT size to the target sample size, we choose among the available profiles those that generate an equal number of LAI samples in a number of 10%-wide LAI bins between the minimum and maximum target LAI values. This ensures that we have the same number of profiles in each of these bins, and therefore that we sample equally profiles that generate different ranges of LAI.
- LUT calculation: the reflectance spectra outputted by the model are convolved using the Spectral Response Function (SRF) of the target sensor.

ML inversion

Machine learning methods saw a surge of interest in the past decade for their ease of implementation and their computational speed after the training phase. Random forest regression (RFR) is an ensemble algorithm based on multiple decision trees with frequent use for functional traits retrieval in remote sensing (Izquierdo-Verdiguier and Zurita-Milla, 2018). The mixture of bootstrapping and random feature selection makes it less sensitive to outliers and noise (Waske et al., 2009). RFRs are out-of-bag predictors, meaning that they can only predict values within the range they were trained (Breiman, 2001). We will use python's scikit-learn package (Pedregosa et al., 2011) to do the conjoint pre-processing, fitting, prediction and evaluation of target variables with RFR. Following (Danner et al., 2021), for RFR, neither the variation of max. features, nor the number of estimators, nor the minimum number of samples per leaf had a notable impact on the model's performance. Best results for estimation of LAI are obtained when 75% of the features are used for training (max. feature = 0.75). A higher number of estimators in the random forest turned out to be slightly beneficial for the training success. The minimum number of samples per leaf for each decision tree turned out to be quite insensitive. The best results with a 2000 combinations LUT (rRMSETest = 0.25, R2Test = 0.82) were obtained (Danner et al., 2021) with the following parameterization:

- Max. features: 0.75
- Min. samples per leaf: 1
- NEstimators: 100+

Max. features did not have any impact on model size, but the minimum number of samples per leaf scaled with inverse potency and could therefore be increased to reduce model size.

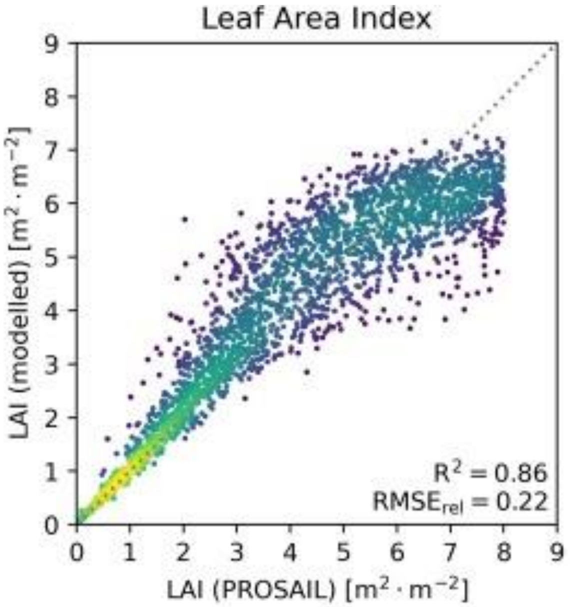

Figure 10. Validation on simulated test data of the best performing RFR parameterizations for each biophysical variable, trained from synthetic LUT5000 by (Danner et al., 2021). Density of scatter points is depicted by colors ranging from purple (sparse) to yellow.

4.4.3. Alternative LAI sources

An alternative source of LAI data requested to feed crop growth model like AQUACROP, which we could use while we collect ground data to develop an approach based on PROSAIL inversion method, is the one provided by the Biophysical Processor implemented in SNAP (Sentinel Application Platform Toolbox).

They method implemented in SNAP consists in generating a comprehensive database of vegetation characteristics and the associated Sentinel-2 top of canopy (TOC) reflectances. Neural networks have been trained to estimate the canopy characteristics from the TOC reflectances along with set corresponding angles defining the observational configuration. Different neural network architectures have been implemented, the NNET 20m and the NNET 10m. They use a different combination of input bands as shown in the table below as input for the neural network in addition to the auxiliary information cos(viewing_zenith), cos(sun_zenith), cos(relative_azimuth_angle).

Table 13. List of bands used by Neural Network methods implemented in the SNAP biophysical processor.

S2 band	Wavelength (µm)	Resolution (m)	NNET 20m	NNET 10m
B3	0.560	10	X	X
B4	0.665	10	X	X

B5	0.704	20	X	
B6	0.740	20	X	
B7	0.783	20	X	
B8	0.842	10		X
B8A	0.865	20	X	
B11	1.610	20	X	
B12	2.190	20	X	

The NNET 10m uses only 10m bands and so it produces a 10m resolution output product, however it is capable of computing only the LAI, FAPAR and FVC indexes.

Both NNET 10m and NNET 20m are composed by three layers:

- one input layer: made of 11 normalized input data for the NNET 20m, 6 for the NNET 10m;
- one hidden layer with 5 neurons with tangent sigmoid transfer functions
- one output layer with a linear transfer function

In the final implementation there are two NNET 20m, one trained with S2A data and one with S2B data, and two NNET 10m, again trained for S2A and S2B respectively. This allows to take in account the small differences in the reflectance response of the different sensors.

The S2 SNAP Toolbox biophysical variable retrieval algorithm is based on specific radiative transfer models associated with strong assumptions, particularly regarding canopy architecture (turbid medium model). All the variables derived from such algorithms should be seen as effective, i.e. the variables that would correspond to the measured satellite signal reflected by a canopy verifying all the assumptions made through the radiative transfer models. he algorithm is "generic", meaning that it should apply to any type of vegetation with a reasonable performance. It is based on methods that have already been proven to be efficient and have been implemented to generate biophysical products from MERIS, SPOT VEGETATION and Landsat sensors (ATBD, 2016).

4.5. Spatiotemporal enhancement of ECOSTRESS imagery

Over this chapter there is a brief presentation of the current state of the art on the discipline of thermal fusion and sharpening algorithms on remote sensing data. Subsequently the methodology that will be followed for the spatiotemporal enhancement of ECOSTRESS thermal data is documented, followed by a description of the service outputs.

4.5.1. Data Fusion on thermal data. A review of state of the art

Land surface temperature (LST), the skin temperature of the Earth surface, is one of the major variables of climate systems, and has been used as a key parameter in modeling surface energy balance (Hain and Anderson, 2017). LST interacts with other factors such as soil moisture, air temperature, and evapotranspiration. In particular, LST has been widely used in investigating various socio-environmental problems.

LST has relatively large variation in both spatial and temporal domains due to the complicated characteristics of environmental factors such as vegetation coverage, topography, soil texture, and land cover patterns, which are closely related to LST. Although in-situ ground measurements provide accurate surface temperature at a location, they do not provide spatially continuous LST information over vast areas. Satellite remote sensing has been a good alternative to spatiotemporal LST delineation from regional to global scale. Thermal infrared (TIR) sensors are a major source for producing satellite-based LSTs under clear sky conditions.

Among various satellite-based LSTs, MODIS LST is the most widely used LST product in modeling atmosphere, ocean and land processes on the Earth thanks to its spatiotemporal coverage and longevity (> 20 years). MODIS sensors onboard Terra and Aqua satellites collect data providing LST four times a day (local solar times of 10:30 am and 10:30 pm for Terra, and 1:30 am and 1:30 pm for Aqua) at 1 km spatial resolution. MODIS LST is generated based on the generalized split-window algorithm and is provided as global grid data at multiple time scales (i.e., daily, eightday, and monthly LSTs).

One of the drawbacks of LST products at relatively coarse spatial resolution (i.e., 1 km) like MODIS LST or Sentinel 3 is that they cannot be used at the context of agricultural studies. With the increasing demand of satellite derived products in various areas under changing climate conditions, information of detailed thermal environment on the Earth surface at high resolution (e.g., 10-100 m) is required (Hulley et al., 2019). In particular, the use of 1 km MODIS LST over urban areas showing very heterogeneous thermal surface characteristics is limited (Yoo et al., 2020).

There are several satellite sensors that globally provide fine resolution (~100 m) LSTs, such as Landsat series and ECOSTRESS. However, their temporal resolutions are relatively low around 16 days, limiting investigation of temporal variation of LSTs. To solve the trade-off between the spatial and temporal resolution of remote sensing-derived products such as LST, many studies have provided spatiotemporal downscaling methods using multi-sensor data. In particular, due to the complexity of thermal landscapes, many factors should be considered when performing thermal downscaling which is also known as thermal sharpening or disaggregating (Weng et al., 2014).

The thermal downscaling of 1 km MODIS LST through a multitude of techniques can generate high spatial resolution daily LST products with medium spatial resolution.

Many approaches for thermal downscaling of MODIS LSTs have been developed during the past decade showing varied performance and efficiency. Each approach has its own merits and limitations, and there are still key challenges that should be carefully addressed in any thermal fusion attempt.

Kernel-driven methods

The kernel-driven method is the most frequently used thermal downscaling approach in recent years. The kernel-driven method spatially aggregates high resolution input variables matching the coarse resolution LST scale, then models the relationship between LSTs and the upscaled input variables. Finally, the method applies the developed model to the original high resolution input variables, called kernels, to produce high resolution LSTs.

In addition, most kernel driven method applied a residual correction process originally suggested by Kustas et al. (2003).This process generally uses the following steps:

1. aggregating the simulated high resolution LST (LSThigh) to the original coarse resolution LST scale
2. subtracting the aggregated LSThigh (LSTag) from original coarse resolution LST (called residuals; Δ)
3. resampling the residuals to LSThigh scale and adding these residuals to the LST high for generating downsampled LST

The spatial resolution of downscaled LST is determined by the resolution of the kernels. There are many factors that affect the performance of the kernel-driven approach, including types of kernels and modeling techniques. Spectral reflectance data at higher spatial resolution (i.e., red and near- infrared -NIR - bands) can be used as kernels for thermal downscaling of LST images produced at the same time. In particular, the normalized difference vegetation index (NDVI) is calculated using the red and NIR bands. Since there is a linear relationship between NDVI and LST, NDVI has been used as a useful kernel for thermal downscaling. This downscaling approach using NDVI is the basic kernel- driven method, which is called the thermal sharpening algorithm (TsHARP).

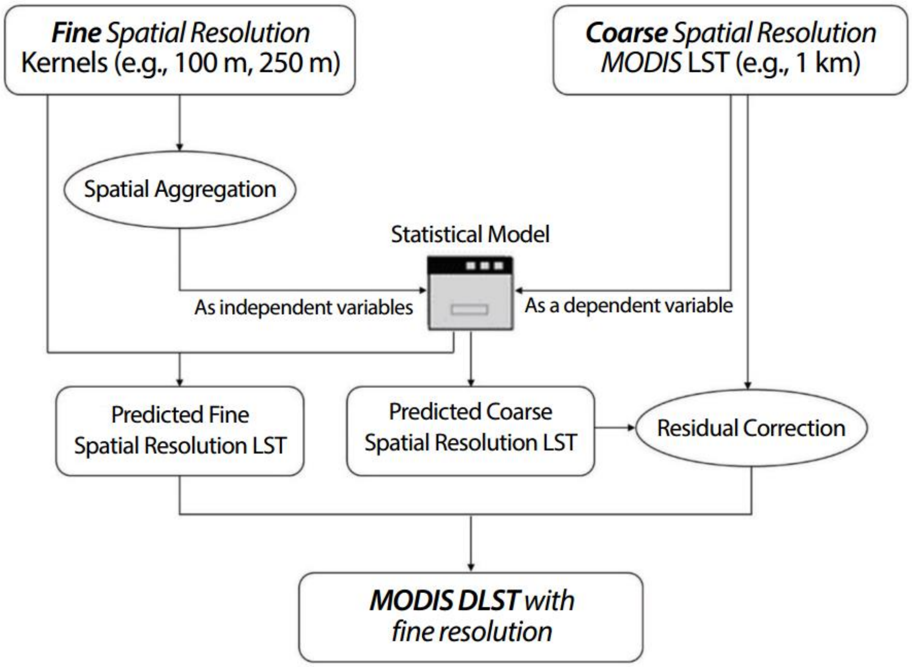

Figure 11. Flowchart of kernel based downsampling of MODIS LST data.

Fusion-based methods

Fusion-based methods determine the relationship between the image pairs (known) of fine resolution LST and coarse resolution LST, and downscale coarse resolution LST (e.g., MODIS LST) when fine resolution LST is not available. Compared to the kernel-driven methods that depend on kernel acquisition time, the fusion-based methods are less restrictive in selecting the target date of Downsampled LST in that they directly model two LST images instead of the relationship between LST and kernels (Xia et al., 2019).

Yin et al. (2021) proposed a deep learning-based spatiotemporal temperature fusion network (STFN), which fuses images based on convolutional neural networks (CNN) handling the non- linearity of LST temporal changes while the existing fusion-based methods used linear models. In their study, STFN produced better performance (RMSEs of 1.40 and 1.28K for two study sites) than other state of the art fusion methods like ESTARFM (RMSEs of 1.90 and 1.49K).

Open issues and challenges in thermal sharpening methods

Various approaches have been proposed to spatially downscale MODIS LST for the past decade. While their performances have gradually improved, there are still challenges and limitations. Major issues and challenges to discuss here are:

- **Uncertainty in LST retrievals**

There are varied LST retrieval algorithms depending on satellite data used (i.e., MODIS, Landsat, and ASTER). MODIS 1 km LST is retrieved using a generalized split-window (GSW) algorithm based on brightness temperature measured at MODIS band 31(10.78-11.28 μm) and 32 (11.77-12.27 μm), and respectively other thermal sensors that map LST like Sentinel 3 or ECOSTRESS have their own LST retrieval model.

Furthermore, each LST product has its own retrieval error, which is another challenge for the accurate evaluation of LST downscaling. Major LST retrieval error sources include the lack of understanding for the effects of atmospheric attenuation, insufficient information of the emissivity, and the uncertainties of input factors used for LST retrievals (Ghent et al., 2019). Emissivity is a critical factor in satellite based LST retrievals. It is well known that small uncertainty in the emissivity (~1%) can result in an LST retrieval error > 1K (Chen et al., 2016). In summary, the inherent errors of satellite-based LSTs that are used for training and validation of downscaling make the objective evaluation of LST downscaling difficult.

- **Low thermal contrast**

The literature shows that downscaled LST has relatively low thermal contrast when compared to high resolution reference LST, which is called blurring effect (Ebrahimy and Azadbakht, 2019; Li et al., 2019). This problem often occurs when the kernel-driven method with machine learning is used for LST downscaling. Most machine learning approaches tend to estimate output to minimize errors, which are related to the distribution range of training data (Yoo et al., 2020).

- **Nonlinearity of LST temporal change**

The fusion-based methods have been gradually developed, but there remain issues where typical fusion based techniques (i.e., STARFM) assume that the output DLST is linearly related to input LSTs. In fact, conventional fusion-based methods assume that the surface cover type and systematic errors do not change much over time because they were originally suggested for downscaling the reflectance. Unfortunately, while reflectance changes slowly with time, LST has rapid temporal change with nonlinearity (Mohamadi et al., 2019). To solve this challenge, some fusion-based studies tried to consider the LST temporal change using the MODIS annual cycle parameters (Weng et al., 2014) or thermal components based on the nonnegative matrix factorization extracted from the Landsat 8 red, near infrared (NIR) and thermal infrared band (Wang et al., 2020). Recently, a fusion approach of LST images was proposed using the non-linear fitting model, such as a deep learning-based CNN (i.e., STTFN; Yin et al., 2021). It should be noted that STFN is able to build up the complicated relationship without manually designed mathematical rules as the conventional fusion models because it can directly model the nonlinear relationship between the input and output LSTs.

- **Cloud contamination**

Thermal infrared (TIR) sensors such as MODIS, Landsat, and ASTER are the most widely used ones to retrieve LSTs. One of the most critical problems when using TIR-derived LSTs is the sensitivity to atmospheric and weather conditions. Unfortunately, LST retrievals from TIR sensors are not available under clouds due to their inability to penetrate clouds (i.e.,cloud contamination).

- **Model generalization**

Most LST downscaling methods developed for the past decade have been evaluated over local areas,which limits the generalization of the proposed methods. The performance of the methods often varied by the characteristics of climate and land cover types (Wang et al., 2020; Yang et al., 2017). One possible solution to ensure LST downscaling approaches to have a generalized capability is to evaluate them over multiple areas with different conditions and optimize the related parameters.

4.5.2. STFN Deep Learning networks for ECOSTRESS thermal images

In the course of AFRI4Cast EO data enhancement, ECOSTRESS LST data will be sharpened with the application of a deep learning based SpatioTemporal Temperature Fusion Network (STFN) method, as described by Wang et al. (2022) and Yin et al. (2021), for the generation of fine spatiotemporal resolution LST products is proposed. In STFN, a multi- scale fusion convolutional neural network will be employed to build the complex nonlinear relationship between input and output LSTs. Thus, unlike other LST spatiotemporal fusion approaches, STFN is able to form potentially complicated relationships through the use of training data without manually designed mathematical rules making it more flexible and intelligent than other methods.

Additionally, two targets fine spatial resolution LST images are predicted and then integrated by a SpatioTemporal-Consistency (STC)-Weighting function to take advantage of spatiotemporal consistency of LST data. A set of analyses using two real LST data sets obtained from ECOSTRESS and Moderate Resolution Imaging Spectroradiometer (MODIS) or Sentinel 3 LST, will be used.

If new acquisitions of the ECOSTRESS cannot be planned, the temporal frequency of the current acquisitions (1-7 days, 4 days on average) will be enhanced to increase the available LST values to a daily frequency. Fusion-based methods determine the relationship between known image pairs of LST, at fine and coarse resolution, and downscale coarse resolution (e.g., MODIS LST) when fine resolution (ECOSTRESS LST) LST is not available. The proposed solution involves the use of a deep learning-based spatiotemporal fusion network (STFN), which fuses images based on convolutional neural networks (CNN) handling the non-linearity of LST temporal changes.

Fusion-based methods determine the relationship between known image pairs of LST, at fine and coarse resolution, and downscale coarse resolution (e.g., MODIS LST) when fine resolution (ECOSTRESS) LST is not available. The proposed solution involves the use of a deep learning-based spatiotemporal fusion network (STFN), which fuses images based on convolutional neural networks (CNN) handling the non-linearity of LST temporal changes.

In STFN, a multi-scale fusion Convolutional Neural Network is employed to build the complex nonlinear relationship between input and output variables. Thus, unlike other spatiotemporal fusion approaches, STFN is able to form potentially complicated relationships through the use of training data without manually designed mathematical rules making it more flexible and intelligent than other methods.

The multi-scale fusion CNN contains three parts:

1. **super-resolution** of temporal change between the input target and neighboring coarse spatial resolution LST images
2. **high-level feature abstraction** of neighboring fine spatial resolution data
3. **integration** of the extracted multi-scale features.

Furthermore, to take advantage of the temporal consistency commonly observed in a series of LST images, the STFN uses two fine-coarse spatial resolution LST image pairs observed before and after the target date to train two multi-scale fusion CNNs, and then combine their predictions using a Spatiotemporal-Consistency (STC)-Weighting function.

Considering the special characteristics of temperature, there are four differences of STFN compared with existing deep learning-based spatiotemporal fusion methods:

- in the super-resolution process, fine spatial resolution image is used to provide fine spatial texture information
- residual learning modules are applied to preserve lost features in the convolution and fuse features at different scales
- in the training process, Huber loss function is used for decreasing the negative influence of noises and outliers,
- In the combination, a STC-weighting strategy which considers spatiotemporal consistency is employed to derive the final result.

ECOSTRESS and MODIS LST data will be used as fine and coarse spatial resolution data, respectively, with Landsat TIRs and Sentinel 3 LST as alternatives.

The aim is to obtain a pair of fine and coarse LST images that pre-date the target date, for which a coarse MODIS image is available, together with another pair of fine and coarse images that post-dating the target date. Then, from one MODIS LST image at the target date and two pairs of ECOSTRESS and MODIS images at the neighboring dates, a high resolution (ECOSTRESS -like) LST image is predicted.

For simplicity, the target date is denoted as t_2, and the dates pre- and post-dating t_2 are denoted as t_1 and t_3, respectively. Accordingly, the MODIS coarse resolution image (LST) at t_2 is denoted as M_2, and the ECOSTRESS-MODIS image pairs (LST) at dates t_1 and t_3 are denoted as E_1 and M_1 and E_3 and M_3, respectively.

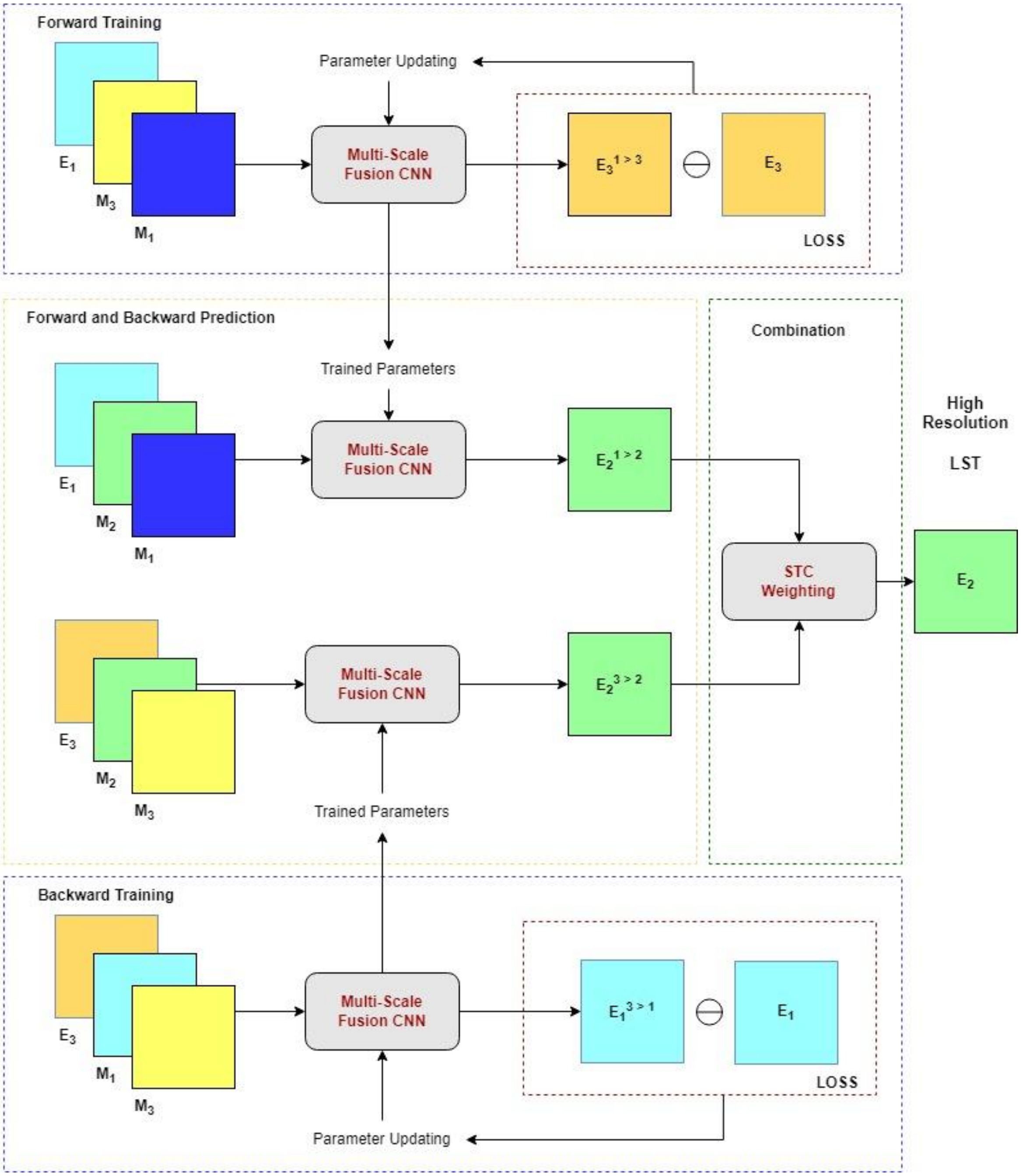

Figure 12. Flowchart of the Spatiotemporal Fusion Network.

As depicted in Fig.12, the proposed STFN generates a fine spatial resolution image via a three-stage process:

1. forward and backward model training
2. forward and backward prediction
3. combination of forward and backward predicted high images to yield a final fine spatial resolution predicted image for t_2

The input fine and coarse spatial resolution images are first preprocessed. Then, a forward multi-scale fusion CNN, which blends E_1, M_1, and M_3 to predict $E_3^{1>3}$, is gradually learned and optimized; the superscript 1>3 indicates forward modeling based on the image pairs at t_1 and t_3. Additionally, an optimally trained backward multi-scale fusion CNN can be obtained by using E_3, M_3 and M_1 to predict $E_1^{3>1}$, the superscript highlights backward modeling. In the prediction stage, two predicted fine spatial resolution LST images, which are expressed as $E_2^{1>2}$ and $E_2^{3>2}$, are generated by the optimal forward and backward multi-scale fusion CNNs, respectively. Then these two layers are combined via a STC-Weighting function.

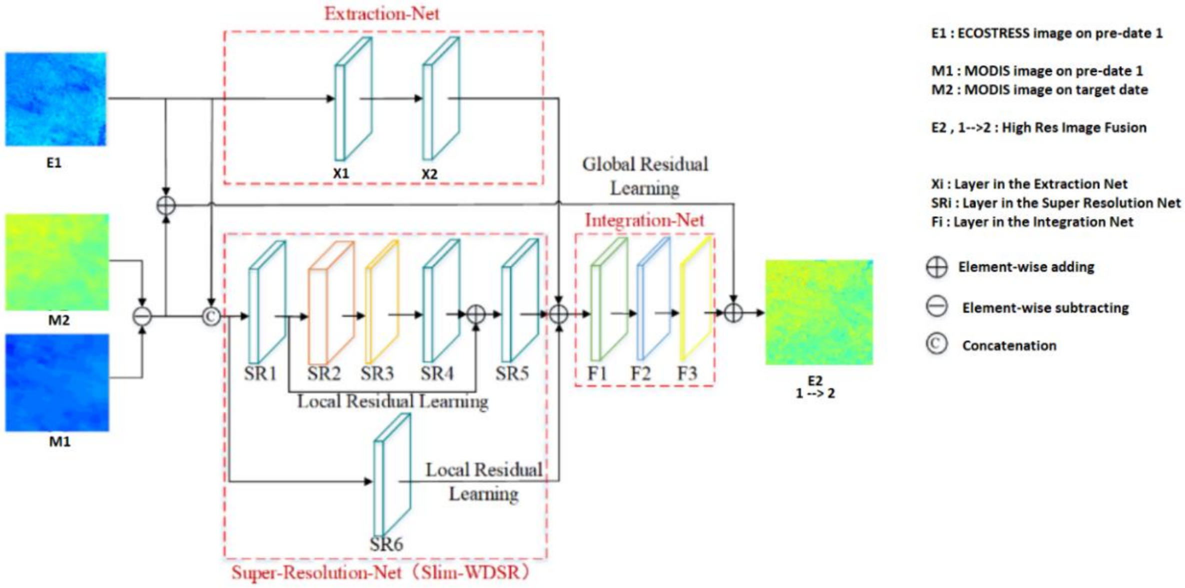

Figure 13. Architecture of Multiscale Fusion CNN.

The architecture of multi-scale fusion CNN is illustrated using the prediction of $E_2^{1>2}$ from E_1, M_1 and M_2 as example (Fig. 13). The multi-scale fusion CNN is a fully convolution network, which enables an end-to-end mapping from three input images to an output high resolution image.

It first extracts high-level features of E_1 and super resolves the change image between M_2 and M_1 at the same time, then fuses and retrieves the extracted feature maps to the fine spatial resolution result. Therefore, the whole architecture of the multi-scale fusion CNN contains three major parts, termed here as

- **Extraction-Net**, a two-layer convolution network employed to extract the high-level features of the ECOSTRESS image and provide fine abundant spatial pattern information for the prediction.
- **Super-Resolution-Net.** The focus in the fusion process is on locating temporal change between the target and neighboring dates. By using a super-resolution module, the coarse spatial resolution pixels of the temporal change (Subtraction) image are disaggregated into fine spatial resolution pixels, which can offer more spatial pattern information. To implement the super-resolution, a modified version of the state-of-the-art super-resolution model "Wide Activation for Efficient and Accurate Image Super-Resolution (WDSR)", (Yu et al., 2018), will be used ,referred to here as slim-WDSR.

- **Integration-Net**, which is made up of three stacked convolutional layers. The generated feature maps are integrated and used to estimate the target image gradually through the Integration-Net

The core components of the Multiscale Fusion CNN are described on the following table.

Table 14. Core components of the Multiscale Fusion CNN.

LAYERS OF THE MULTI-SCALE FUSION CNN					
Extraction-Net		**Super-Resolution-Net**		**Integration-Net**	
level	**layer**	**level**	**layer**	**level**	**layer**
X1	conv 3×3, 32, Batch Normalization, ReLU	**SR1**	conv 3×3, 32	**F1**	conv 3×3, 32, Batch Normalization, ReLU
X2	conv 3×3, 32	**SR2**	conv 1×1, 64, Batch Normalization, ReLU	**F2**	conv 3×3, 16, Batch Normalization, ReLU
		SR3	conv 1×1, 25, Batch Normalization, ReLU	**F3**	conv 3×3, 1
		SR4	conv 1×1, 32, Batch Normalization, ReLU		
		SR5	conv 3×3, 32, Batch Normalization, ReLU		
		SR6	conv 3×3, 32		

4.5.3. Service outputs

The ECOSTRESS spatiotemporal enhancement component will use the proposed methodology in order to deliver to AFRI4Cast the following product services:

Daily Land Surface Temperature at a spatial resolution of 70 m. If day/night ECOSTRESS LST acquisitions are found, over the pilot areas, at a proper revisit interval, the STFN will produce dual LST layers. Considering the ECOSTRESS revisit period, as 2 temporal instances D_i and D_n, where i goes from 1 to n, spatiotemporal enhancement component will produce daily LST layers d_1,d_2,..,d_n with a pixel size of 70 m.

4.6. Copernicus Sentinel-2- Crop monitoring services

Crop monitoring services based on Copernicus Sentinel-2 data will serve as a subsidiary service. This service will act complementary to the field data in case of field data insufficiency as, apart for correcting geolocation of PRISMA imagery, Sentinel-2 images are also used to compute on a yearly basis:

- Crop type maps;
- Crop phenology assessment and
- Crop phenology monitoring maps;

4.6.1. Crop type maps

Various vegetation types have different growth behaviors and thus different characteristics of NDVI time series curves. Then, classification methods based on multi-temporal image series have been well acknowledged in agriculture, since crop systems usually disclose specific and often separable seasonal trends, within a particular agro-ecological area, during the annual cycle (Mather and Tso, 2009; Pax Lenney et al., 1996). As a rule, taking advantage of a large number of sequential multi-temporal images assures to effectively describe the crop seasonality. Nevertheless, when the number of time-series images is too large and significant correlation among them exists, the dataset becomes redundant: additional images add little information but increase the computing complexity. In the field of signal detection and signal matching applications time series methods that can be classified as time-domain or frequency-domain, are commonly used: the former ones use mathematical tools such as autocorrelations, cross-correlations and convolutions(Quiero et al., 2015). A phenology-based classification (PBC) approach has been developed and tested, which doesn’t need to model NDVI variation with some logistic or double sigmoid fitting function because the discriminating agent will be the degree of cross-correlation of the interpolated phenology profiles. In fact, cross-correlation is widely used as effective similarity measure in matching tasks, to be able to discriminate for different crop species using Sentinel-2 MSI imagery.

The first step of the crop mapping procedure is the co-registration of the entire image collection to evaluate the NDVI, masking out all the pixels that are cloudy or not vegetated or saturated, using the scene classification map provided by Sentinel-2. Each Sentinel-2 L2A image includes a classification map (SCL, Scene Classification) at 20 meters resolution which provides a first coarse classification, that gives preliminary information such as vegetated/not-vegetated pixel, cloudy/not-cloudy, and makes possible a first data-sanitation process. To discriminate crop species using phenology, profiles of the characteristic crops of the area of interest are necessary, so a training dataset is needed to retrieve from the selected training points and from the time series images the reference phenologies for each crop type. These data are used to implement a set of reference phenologies to be used during the cross-correlation comparison in the classification process. The overall process is outlined in Figure 14.

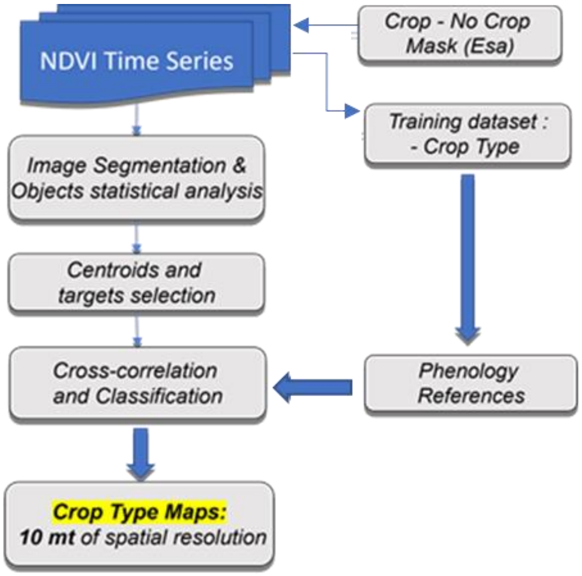

Figure 14. Outline of the overall classification process (Saquella et al., 2022).

On one side of the chain the training dataset is processed to obtain the reference library needed for the comparison, performing a statistical analysis on each polygon-like crop field and extracting for each polygon the mean value and standard deviation with the aim of extrapolate a single characteristic and representative phenology profile for the whole crop field, taking advantage of the crop calendars as first references in the assessment of the phenology profiles. On one side of the chain the training dataset is processed to obtain the reference library needed for the comparison, performing a statistical analysis on each polygon-like crop field and extracting for each polygon the mean value and standard deviation with the aim of extrapolate a single characteristic and representative phenology profile for the whole crop field, taking advantage of the crop calendars as first references in the assessment of the phenology profiles.

On the other side of the processing chain all the crop fields are investigated and detected. The procedure goes through several steps. Firstly, selecting the best and the clearest NDVI images, a multi-image edge detection and a subsequent watershed algorithm were applied to get the image segmentation. This crucial step can be improved in the preprocessing phase with an aggregation of multiple canny edge detection images on cloud-free images, with subsequent morphological transformations such as small objects removal, filling holes, dilation and thinning to clean the noise (Figure 15). Once all the crop fields are recognized and represented as isolated homogeneous objects, a statistical and morphological analysis is carried out to find and isolate a single target pixel which will be representative of the whole field analyzing its spectral variability over its geometry (Luciani et al., 2021). Centroids are representative of objects geometry (being the arithmetic mean of all pixels within the objects), and the target points are selected as the closest pixels to the centroids, included within the field polygon perimeter. Target point phenology is derived by statistically analyzing a region of pixels centered around it, for example a 10-by-10 pixels square around the target point within the object, so that it is considered the phenology variability across a good part of the field. For classification purposes this simplification seems enough to reduce the computational time over wide areas, retaining a good accuracy provided by the previous segmentation.

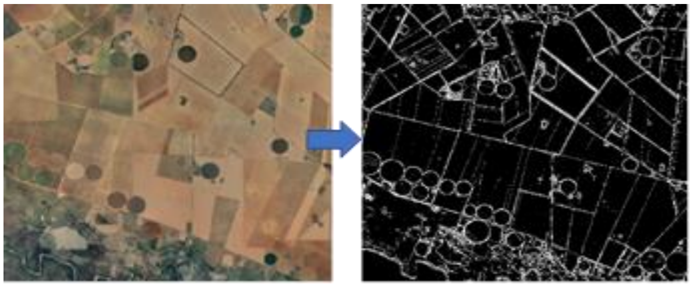

Figure 15. Multi image Edge detection (Bothaville, South Africa, 2021) (Saquella et al., 2022)

The processing chain goes on with the phenology extraction step. After masking out all the out of bounds crops outside the cropland areas of the ESA World Land Cover mask, for each crop target pixel the NDVI behaviour is extracted over a year and averaged over the centroid's region. Then, NDVI series is interpolated in time using a Modified Akima cubic Hermit interpolation method to avoid overshoots in the building process of phenology profiles.

Each target crop within the crop mask will be classified by its centroid's region associated phenology. A cross-correlation sequence among the target crops phenology and the reference phenologies measures the degree of similarity among them. By means of cross-correlation comparison, the crop type is found when the best match occurs, looking for the highest correlation value associated with the minimum time lag, choosing properly a set of thresholds to be applied on correlation and lag values, beyond which no class is associated to the target crop (Luciani et al., 2021).

An example of crop map obtained by using the above described procedure is shown in Figure 16.

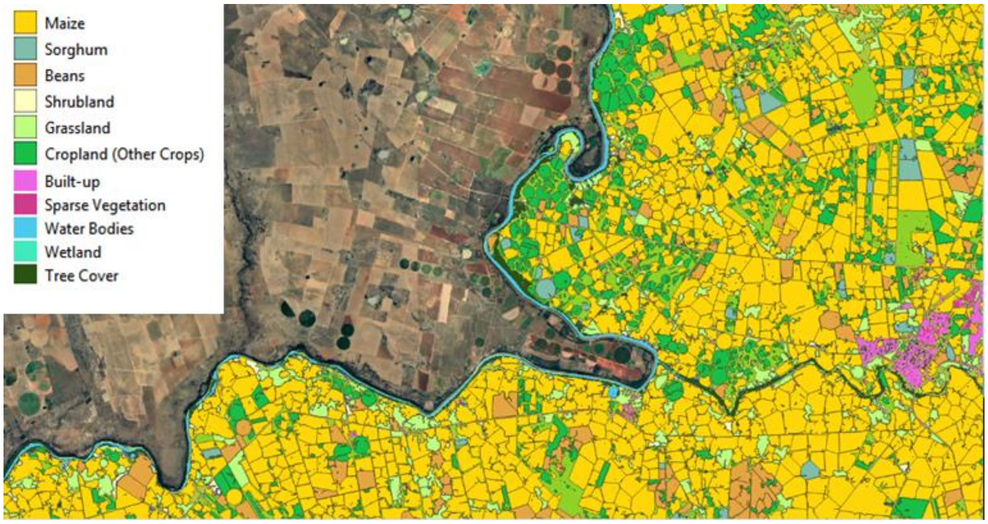

Figure 16. Crop type map.

Algorithm Outline/Flow Chart

The NDVI time series is computed by using the Sentinel-2 images. A time series of one year of images is used to extract the key parameters characterizing different phenological cycle associated with different crop types.

The main crops of interest as far as selected are listed below:

- Wheat
- Maize
- Rice

The processing chain in AFRI4Cast crop phenology monitoring is mainly composed of the following stages:

1. Near real time collection of NDVI maps
2. Download of EO data and image processing.
3. Extraction of phenology characterizing parameters (Fig 17.)
4. NDVI time series analysis and parameter retrieval. Phenological signatures are retrieved as the situation on the ground is under development. As long as the phenological signature is incomplete, only a partial comparison can be carried out with the reference signature.
5. Cross-correlation based classification procedure.

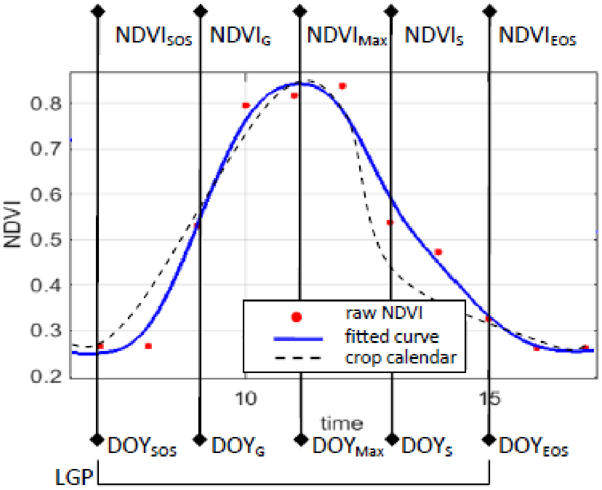

Figure 17. NDVI values of summer wheat at the transition dates describing the key points of the phenological development of a crop species; the phenological curve has been retrieved from the NDVI raw values and the compared with reference phenology from FAO crop calendar.

4.6.2. Crop phenology assessment

Crop phenology assessment and monitoring services aim at:

- assessing the crop growth behaviour by comparing the actual vegetation index (NDVI or LAI) with the expected behaviour based on reference phenology for crops present in the area of interest or previous year crop phenology parameters;
- assessing spatio-temporal variability in cropping fields; and
- detecting any change in the phenology of the crop by comparing the most recent phenology parameters extracted by using the satellite image time series with the reference calendar, or the previous year phenology.

Therefore, these two services, based on Sentinel-2 images, allows to assess the crop behavior and monitor changes in the phenology of the crops, if any. The change of course could be due to a change in the type of crop present in the pixel, or seasonal growth changes as reaction to climate changes. Concerning possible changes due to crop rotation or changes in the land use this could be assessed by looking at the updated crop type map.

Spatial variability in crop yield is the result of complex interaction of factors influencing crop growth that include soil (such as nutrients, soil water availability), topographical factors (such as elevation) and climatic factors (such as rainfall and temperature). In addition to their spatial variability, some of these factors such as climate have temporal variability, which causes the spatial pattern of crop yield to vary from season to season.

Remote sensing vegetation indices have potential to assess crop growth variability by quantifying relative growth and health condition of the crop. Remote sensing phenology estimates phenological growth stages including the start of season and end of season from multi-temporal vegetation index data. The derived metrics may not necessarily correspond directly to conventional, ground-based phenological events, but they provide important information about the vegetation growth dynamics that can be associated with environmental factors such as soil properties and meteorological conditions.

Input

1. Map of the agro-ecologic zones.
2. Crop type map
3. Existing crop calendar map
4. Sentinel-2 images.

Output

The crop phenology assessment provides a 7-band raster, in geotiff format. The 7 bands of the geotiff file contain (see Table 15.):

i. key parameters of the phenology associated with each pixel corresponding to agricultural areas, based on annual time series of Vegetation Index computation, that are: SOS (Start Of Season), EOS (End Of Season), DOYM (day of the NDVImax), and CropType.
ii. Indication on the season: first or second season.

The map will be updated every year.

Table 15. List of variables contained in the output file of the crop phenology assessment product.

Type of Data	Parameter	Spatial Resolution	Temporal Resolution	Units	Range
Start of Season 1	*SOS1*	*10 m*	*Annual*	*dekad*	*0 – 72*
Day of max NDVI 1	*DOYM1*	*10 m*	*Annual*	*dekad*	*0 – 72*
End of Season 1	*EOS1*	*10 m*	*Annual*	*dekad*	*0 - 72*
Start of Season 2	*SOS2*	*10 m*	*Annual*	*dekad*	*0 – 72*
Day of max NDVI 2	*DOYM2*	*10 m*	*Annual*	*dekad*	*0 – 72*
End of Season 2	*EOS2*	*10 m*	*Annual*	*dekad*	*0 - 72*
Crop Type	*CT*	*10 m*	*Annual*	*dimensionless*	*Int 0:255*

Methodology

Phenological profiles provide historical NDVI projection over a specific site and can be used to discriminate for different crop species and to identify crop rotation cycles and biomass seasonal trends. The overall algorithm outline/flow chart is presented in Figure 18.

An object-based algorithm has been designed to automatically retrieve vegetation phenological metrics starting from NDVI time series. The NDVI values from cloud are to be excluded filtering the time series with the scene classification map provided by sentinel-2 data, and the missing values over the year are covered interpolating the available NDVI values.

The NDVI time series of the reference dataset used for crop mapping are determined by interpolating the raw NDVI datasets. After filtering outliers and smoothing with rolling mean and extracting the upper envelope of the growing stage, the phenological function were then analysed to retrieve the phenological metrics. For each object already classified, it was stored the corresponding reference phenology that has the best matching. Using this a-priori information from the crop type map and the reference phenology that best matches every curve and knowing the cross-correlation lag and all the phenological parameters of the reference phenology it is possible to calculate for each crop field the start of the season and the end of the season. Vegetation development is well described by the following phenological metrics:

The following parameters are meant to be stored:

- DOYS,
- DOYE and
- DOYMax (describing SOS, EOS and NDVI Max respectively), correspond to local minimum or maximum of the phenological function (first derivative equals to zero).

Algorithm Outline/Flow Chart

Algorithms to assess phenology are outlined as it follows:

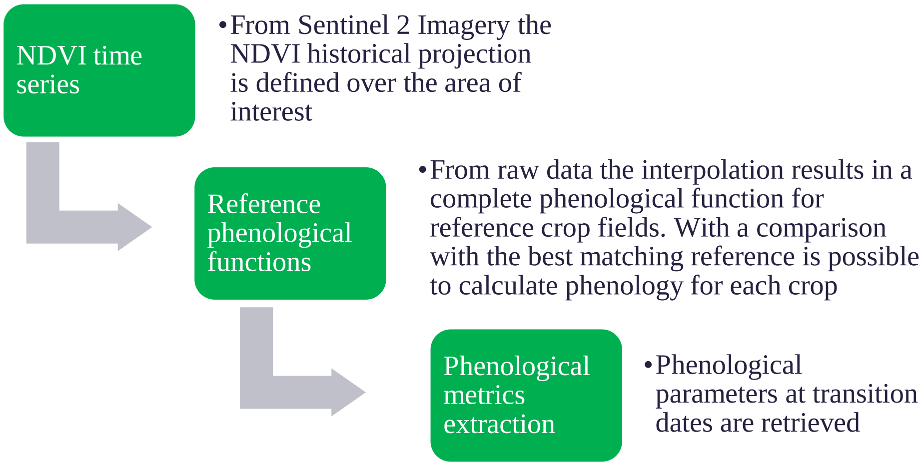

- From Sentinel 2 Imagery the NDVI historical projection is defined over the area of interest
- From raw data the interpolation results in a complete phenological function for reference crop fields. With a comparison with the best matching reference is possible to calculate phenology for each crop
- Phenological parameters at transition dates are retrieved

Figure 18. Crop Phenology assessment algorithm outline.

4.6.3. Crop phenology monitoring

As already mentioned in chapter 4.6.2., crop phenology and monitoring services target on the evaluation of crop growth behavior by comparing the actual vegetation index (NDVI or LAI) with the anticipated behavior based on reference phenology for crops present in the area of interest or previous year crop phenology parameters. The evaluation of spatiotemporal variability in cropping fields as well as the detection of any change in the phenology of the crop are also aspects of the same service.

Output

The crop phenology monitoring provides, at 5 or 10 days frequency, a 2-band raster, in geotiff format. The geotiff file contains: band 1 = difference between the day of the year of the actual NDVI and the nearest day of the previous year with this NDVI value (as described in the methodology), band 2 = time reference: -1, the actual day is antecedent the DOYG; +1, the actual day is later the DOYG.

Changes in vegetation phenology may in turn alter land ecosystem productivity. The phenology assessment service is designed for quantifying shifts in plant phenology in response to climate and seasonal change.

The phenology assessment procedure takes place with respect to a reference phenology derived from crop calendar or from the phenology monitoring services. The assessment procedure takes place on an object base in near-real time.

The Overall algorithm outline/flow chart is presented in Figure 20. The actual NDVI value is retrieved, from the last Sentinel-2 image, over the area of interest, then stored and compared with the reference phenology or last available phenology. Two layers are then provided.

A pixel-based data vector is stored with NDVI values and the associated DOY as soon as they have been acquired. Each NDVI-DOY couple is compared according to the following procedure:

1. Using FAO crop calendar, we can exclude the pixels that correspond to crops out of the current season, considering only the growing season for the following calculations.
2. The nearest day of the previous year with the same value of NDVI as the actual one is computed interpolating over the reference phenology (Figure 19).
3. The value of the sign of this difference is saved at +1 for early growth and -1 for late growth from the previous year.

Finally, we note that the comparison takes place when the phenological signature of the actual observation has not yet classified: in the ascending section of the phenological function in particular, there’s no way to ascertain the crop type under observation and we can only proceed assuming that we are observing the same phenological development of the previous year (that is, the same crop type).

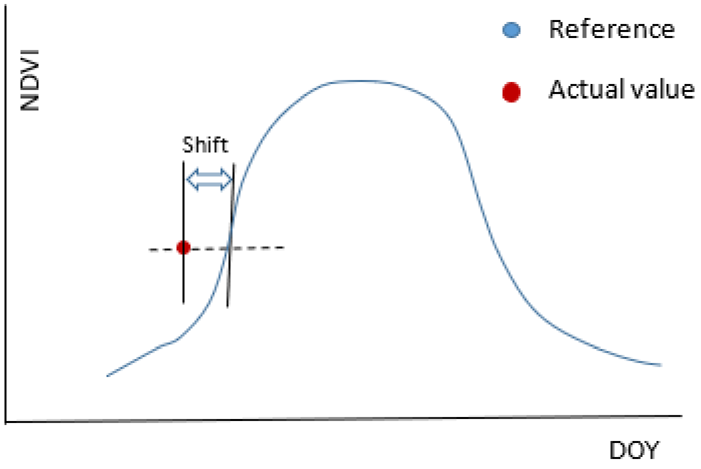

Figure 19. An example of Actual NDVI value comparison with respect to the reference phenology previously monitored.

Algorithm Outline/Flow Chart

Algorithms to monitor phenology are outlined as it follows:

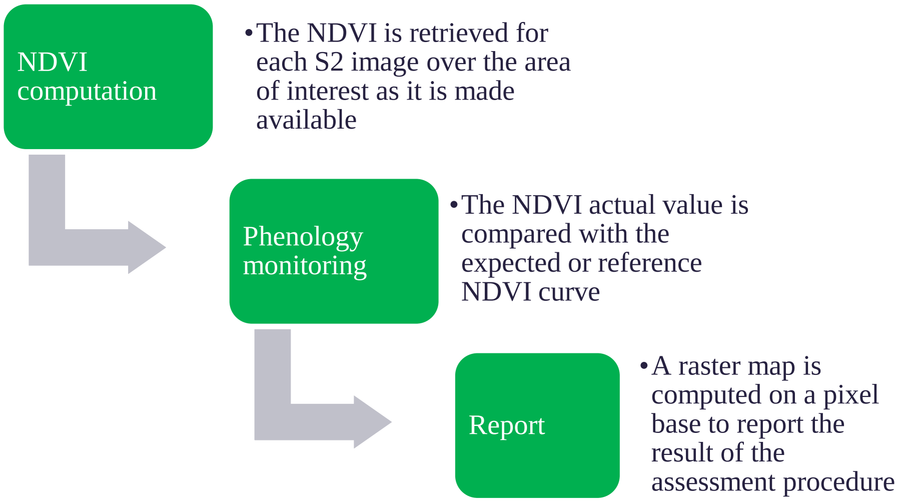

- The NDVI is retrieved for each S2 image over the area of interest as it is made available
- The NDVI actual value is compared with the expected or reference NDVI curve
- A raster map is computed on a pixel base to report the result of the assessment procedure

Figure 20. Crop Phenology monitoring algorithm outline.

5. References

Acito, N., Diani, M., Corsini, G., 2022. PRISMA Spatial Resolution Enhancement by Fusion with Sentinel-2 Data. IEEE J. Sel. Top. Appl. Earth Obs. Remote Sens. 15, 62–79. https://doi.org/10.1109/JSTARS.2021.3132135

Aiazzi, B., Alparone, L., Baronti, S., Garzelli, A., Selva, M., 2012. Twenty-Five Years of Pansharpening A Critical Review and New Developments, in: Signal and Image Processing for Remote Sensing. CRC Press, pp. 533–548.

Anderson, M.C., Yang, Yang, Xue, J., Knipper, K.R., Yang, Yun, Gao, F., Hain, C.R., Kustas, W.P., Cawse-Nicholson, K., Hulley, G., Fisher, J.B., Alfieri, J.G., Meyers, T.P., Prueger, J., Baldocchi, D.D., Rey-Sanchez, C., 2021. Interoperability of ECOSTRESS and Landsat for mapping evapotranspiration time series at sub-field scales. Remote Sens. Environ. 252, 112189. https://doi.org/10.1016/j.rse.2020.112189

Andres Quiero, F., Bennun, L, Quiero+, F., Quintana, F., Bennun, Leonardo, 2015. A novel method based on cross correlation maximization, for pattern matching by means of a single parameter. Application to the human voice. https://doi.org/https://doi.org/10.48550/arXiv.1503.03022

Bochenek, Z., Dąbrowska-Zielińska, K., Gurdak, R., Niro, F., Bartold, M., Grzybowski, P., 2017. Validation of the LAI biophysical product derived from Sentinel-2 and Proba-V images for winter wheat in western Poland. Geoinf. Issues 9, 15–26.

Breiman, L., 2001. Random Forests.

Brown, L.A., Fernandes, R., Djamai, N., Meier, C., Gobron, N., Morris, H., Canisius, F., Bai, G., Lerebourg, C., Lanconelli, C., Clerici, M., Dash, J., 2021. Validation of baseline and modified Sentinel-2 Level 2 Prototype Processor leaf area index retrievals over the United States. ISPRS J. Photogramm. Remote Sens. 175, 71–87. https://doi.org/10.1016/j.isprsjprs.2021.02.020

Busetto, L., Ranghetti, L., 2018. MODIStsp : A Tool for Automatic Preprocessing of MODIS Time Series.

Cawse-Nicholson, K., Anderson, M., 2021a. ECOsystem Spaceborne Thermal Radiometer Experiment on Space Station (ECOSTRESS) ECOSTRESS Level-3 DisALEXI-JPL Evapotranspiration (ECO3ETALEXI) Algorithm Theoretical Basis Document.

Cawse-Nicholson, K., Anderson, M., 2021b. ECOsystem Spaceborne Thermal Radiometer Experiment on Space Station (ECOSTRESS) ECOSTRESS Level-4 DisALEXI-JPL Evaporative Stress Index (ECO4ESIALEXI) Algorithm Theoretical Basis Document National Aeronautics and Space Administration.

Chang, C.I., 2007. Hyperspectral Data Exploitation: Theory and Applications. Wiley, Hoboken, NJ, USA.

Chen, F., Yang, S., Su, Z., Wang, K., 2016. Effect of emissivity uncertainty on surface temperature retrieval over urban areas: Investigations based on spectral libraries. ISPRS J. Photogramm. Remote Sens. 114, 53–65. https://doi.org/10.1016/j.isprsjprs.2016.01.007

Danner, M., Berger, K., Wocher, M., Mauser, W., Hank, T., 2021. Efficient RTM-based training of machine learning regression algorithms to quantify biophysical & biochemical traits of agricultural crops. ISPRS J. Photogramm. Remote Sens. 173, 278–296. https://doi.org/10.1016/j.isprsjprs.2021.01.017

Delalieux, S., Zarco-Tejada, P.J., Tits, L., Bello, M.A.J., Intrigliolo, D.S., Somers, B., 2014. Unmixing-Based Fusion of Hyperspatial and Hyperspectral Airborne Imagery for Early Detection of Vegetation Stress. IEEE J. Sel. Top. Appl. Earth Obs. Remote Sens. 7, 2571–2582. https://doi.org/10.1109/JSTARS.2014.2330352

Dian, R., Li, S., Guo, A., Fang, L., 2018. Deep Hyperspectral Image Sharpening. IEEE Trans. Neural Networks Learn. Syst. 29, 5345–5355. https://doi.org/10.1109/TNNLS.2018.2798162

Dian, R., Li, S., Kang, X., 2021a. Regularizing Hyperspectral and Multispectral Image Fusion by CNN Denoiser. IEEE Trans. Neural Networks Learn. Syst. 32, 1124–1135. https://doi.org/10.1109/TNNLS.2020.2980398

Dian, R., Li, S., Sun, B., Guo, A., 2021b. Recent advances and new guidelines on hyperspectral and multispectral image fusion. Inf. Fusion 69, 40–51. https://doi.org/10.1016/j.inffus.2020.11.001

Ebrahimy, H., Azadbakht, M., 2019. Downscaling MODIS land surface temperature over a heterogeneous area: An investigation of machine learning techniques, feature selection, and impacts of mixed pixels. Comput. Geosci. 124, 93–102. https://doi.org/10.1016/j.cageo.2019.01.004

Eismann, M.T., Hardie, R.C., 2005. Hyperspectral resolution enhancement using high-resolution multispectral imagery with arbitrary response functions. IEEE Trans. Geosci. Remote Sens. 43, 455–465. https://doi.org/10.1109/TGRS.2004.837324

EUMETSAT LSA SAF, 2022. Product User Manual Land Surface Temperature (LST) PRODUCTS: LSA-004 (MLST_DIR), LSA-003 (DLST), LSA-002 (EDLST), LSA-005 (MLST-AS).

EUMETSAT LSA SAF, 2016. Product User Manual Reference Evapotranspiration (DMETREF) PRODUCTS: LSA-303 (DMETREF).

EUMETSAT Satellite Application Facility on Support to Operational Hydrology and Water Management, 2017. Product User Manual (PUM)for product H03B – P-IN-GRU-SEVIRIPrecipitation rate at ground by GEO/IR supported by LEO/MW.

Fisher, J.B., 2018a. ECOsystem Spaceborne Thermal Radiometer Experiment on Space Station (ECOSTRESS) Level-3 Evapotranspiration L3(ET_PT-JPL) Algorithm Theoretical Basis Document.

Fisher, J.B., 2018b. ECOsystem Spaceborne Thermal Radiometer Experiment on Space Station (ECOSTRESS) Level-4 Evaporative Stress Index L4(ESI_PT-JPL) Algorithm Theoretical Basis Document.

Fisher, J.B., 2018c. ECOsystem Spaceborne Thermal Radiometer Experiment on Space Station (ECOSTRESS) Level-4 Water Use Efficiency L4(WUE) Algorithm Theoretical Basis Document.

Fisher, J.B., Lee, B., Purdy, A.J., Halverson, G.H., Dohlen, M.B., Cawse-Nicholson, K., Wang, A., Anderson, R.G., Aragon, B., Arain, M.A., Baldocchi, D.D., Baker, J.M., Barral, H., Bernacchi, C.J., Bernhofer, C., Biraud, S.C., Bohrer, G., Brunsell, N., Cappelaere, B., Castro-Contreras, S., Chun, J., Conrad, B.J., Cremonese, E., Demarty, J., Desai, A.R., De Ligne, A., Foltýnová, L., Goulden, M.L., Griffis, T.J., Grünwald, T., Johnson, M.S., Kang, M., Kelbe, D., Kowalska, N., Lim, J.H., Maïnassara, I., McCabe, M.F., Missik, J.E.C., Mohanty, B.P., Moore, C.E., Morillas, L., Morrison, R., Munger, J.W., Posse, G., Richardson, A.D., Russell, E.S., Ryu, Y., Sanchez-Azofeifa, A., Schmidt, M., Schwartz, E., Sharp, I., Šigut, L., Tang, Y., Hulley, G., Anderson, M., Hain, C., French, A., Wood, E., Hook, S., 2020. ECOSTRESS: NASA’s Next Generation Mission to Measure Evapotranspiration From the International Space Station. Water Resour. Res. 56. https://doi.org/10.1029/2019WR026058

Ghent, D., Veal, K., Trent, T., Dodd, E., Sembhi, H., Remedios, J., 2019. A New Approach to Defining Uncertainties for MODIS Land Surface Temperature. Remote Sens. 11, 1021. https://doi.org/10.3390/rs11091021

Guarini, R., Loizzo, R., Facchinetti, C., Longo, F., Ponticelli, B., Faraci, M., Dami, M., Cosi, M., Amoruso, L., De Pasquale, V., Taggio, N., Santoro, F., Colandrea, P., Miotti, E., Di Nicolantonio, W., 2018. PRISMA hyperspectral mission products, in: International Geoscience and Remote Sensing Symposium (IGARSS). Institute of Electrical and Electronics Engineers Inc., pp. 179–182. https://doi.org/10.1109/IGARSS.2018.8517785

Hain, C.R., Anderson, M.C., 2017. Estimating morning change in land surface temperature from MODIS day/night observations: Applications for surface energy balance modeling. Geophys. Res. Lett. 44, 9723–9733. https://doi.org/10.1002/2017GL074952

Herman, J., Usher, W., 2017. SALib: An open-source Python library for Sensitivity Analysis. J. Open Source Softw. 2, 97. https://doi.org/10.21105/joss.00097

Hook Simon, the ECOSTRESS Team, 2017. ECOsystem Spaceborne Thermal Radiometer Experiment on Space Station.

Houlès, V., Guérif, M., Mary, B., 2007. Elaboration of a nitrogen nutrition indicator for winter wheat based on leaf area index and chlorophyll content for making nitrogen recommendations. Eur. J. Agron. 27, 1–11. https://doi.org/10.1016/j.eja.2006.10.001

Hulley, G., Shivers, S., Wetherley, E., Cudd, R., 2019. New ECOSTRESS and MODIS Land Surface Temperature Data Reveal Fine-Scale Heat Vulnerability in Cities: A Case Study for Los Angeles County, California. Remote Sens. 11, 2136. https://doi.org/10.3390/rs11182136

Hulley, G.C., Göttsche, F.M., Rivera, G., Hook, S.J., Freepartner, R.J., Martin, M.A., Cawse-Nicholson, K., Johnson, W.R., 2022. Validation and Quality Assessment of the ECOSTRESS Level-2 Land Surface Temperature and Emissivity Product. IEEE Trans. Geosci. Remote Sens. 60. https://doi.org/10.1109/TGRS.2021.3079879

Hulley, G.C., Hook, S.J., 2018a. ECOSTRESS LEVEL-2 CLOUD ATBD.

Hulley, G.C., Hook, S.J., 2018b. ECOSTRESS LEVEL-2 Land Surface Temperature and Emissivity Algorithm Theoretical Basis Document (ATBD).

Izquierdo-Verdiguier, Zurita-Milla, 2018. Use of guided regularized random forest for biophysical parameter retrieval. IEEE Int. Geosci. Remote Sens. Symp. https://doi.org/10.1109/igarss.2018.8517920

Justice, C.O., Vermote, E., Townshend, J.R.G., Defries, R., Roy, D.P., Hall, D.K., Salomonson, V. V, Privette, J.L., Riggs, G., Strahler, A., Lucht, W., Myneni, R.B., Knyazikhin, Y., Running, S.W., Nemani, R.R., Wan, Z., Huete, A.R., Leeuwen, W. Van, Wolfe, R.E., Giglio, L., Muller, J., Lewis, P., Barnsley, M.J., 1998. The Moderate Resolution Imaging Spectroradiometer (MODIS): Land Remote Sensing for Global Change Research. IEEE Trans. Geosci. Remote Sens. 36, 1228–1249. https://doi.org/10.1109/36.701075

Kganyago, M., Mhangara, P., Adjorlolo, C., 2021. Estimating crop biophysical parameters using machine learning algorithms and sentinel-2 imagery. Remote Sens. 13, 1–21. https://doi.org/10.3390/rs13214314

Kganyago, M., Mhangara, P., Alexandridis, T., Laneve, G., Ovakoglou, G., Mashiyi, N., 2020. Validation of sentinel-2 leaf area index (LAI) product derived from SNAP toolbox and its comparison with global LAI products in an African semi-arid agricultural landscape. Remote Sens. Lett. 11, 883–892. https://doi.org/10.1080/2150704X.2020.1767823

Kustas, W.P., Norman, J.M., Anderson, M.C., French, A.N., 2003. Estimating subpixel surface temperatures and energy fluxes from the vegetation index–radiometric temperature relationship. Remote Sens. Environ. 85, 429–440. https://doi.org/10.1016/S0034-4257(03)00036-1

Li, W., Ni, L., Li, Z.-L., Duan, S.-B., Wu, H., 2019. Evaluation of Machine Learning Algorithms in Spatial Downscaling of MODIS Land Surface Temperature. IEEE J. Sel. Top. Appl. Earth Obs. Remote Sens. 12, 2299–2307. https://doi.org/10.1109/JSTARS.2019.2896923

Luciani, R., Laneve, G., Orsi, R., 2021. Phenology-Based Classification of Crop Fields Using Cross-Correlation: A Case Study, in: 2021 IEEE International Geoscience and Remote Sensing Symposium IGARSS. IEEE, pp. 1–3. https://doi.org/10.1109/IGARSS47720.2021.9553719

Mather, P., Tso, B., 2009. Classification Methods for Remotely Sensed Data. CRC Press. https://doi.org/10.1201/9781420090741

Mike, S., Sebastien, L., 2018. ECOsystem Spaceborne Thermal Radiometer Experiment on Space Station: Level-1B Resampling and Geolocation Algorithm Theoretical Basis Document (ATBD).

Mohamadi, B., Chen, S., Balz, T., Gulshad, K., McClure, S.C., 2019. Normalized Method for Land Surface Temperature Monitoring on Coastal Reclaimed Areas. Sensors 19, 4836. https://doi.org/10.3390/s19224836

Pampanoni, V., Laneve, G., Santilli, G., 2022. Evaluating Sentinel-3 Viability for Vegetation Canopy Monitoring and Fuel Moisture Content Estimation, in: IGARSS 2022 - 2022 IEEE International Geoscience and Remote Sensing Symposium. IEEE, pp. 5634–5637. https://doi.org/10.1109/IGARSS46834.2022.9884150

Pax Lenney, M., Woodcock, C.E., Collins, J.B., Hamdi, H., 1996. The Status of Agricultural Lands in Egypt: The Use of Multitemporal NDVI Features Derived from Landsat TM. Remote Sens. Environ. 56, 8–20.

Pedregosa FABIANPEDREGOSA, F., Michel, V., Grisel OLIVIERGRISEL, O., Blondel, M., Prettenhofer, P., Weiss, R., Vanderplas, J., Cournapeau, D., Pedregosa, F., Varoquaux, G., Gramfort, A., Thirion, B., Grisel, O., Dubourg, V., Passos, A., Brucher, M., Perrot andÉdouardand, M., Duchesnay, andÉdouard, Duchesnay EDOUARDDUCHESNAY, Fré., 2011. Scikit-learn: Machine Learning in Python. J. Mach. Learn. Res. 12, 2825–2830.

Priya, K., Rajkumar, K.K., 2022. Hyperspectral and Multispectral Image Fusion Using Deep Convolutional Neural Network - ResNet Fusion, in: Hyperspectral Imaging - A Perspective on Recent Advances and Applications [Working Title]. IntechOpen. https://doi.org/10.5772/intechopen.105455

R. Loizzo, R. Guarini, F. Longo, T. Scopa, R. Formaro, C. Facchinetti, G. Varacalli, 2018. PRISMA: THE ITALIAN HYPERSPECTRAL MISSION. IEEE. https://doi.org/10.1109/IGARSS.2018.8518512

Running, S.W., Mu, Q., Zhao, M., Moreno, A., 2019. MODIS Global Terrestrial Evapotranspiration (ET) Product (NASA MOD16A2/A3) Algorithm Theoretical Basis Document Collection 6 1–40.

Saltelli, A., 2002. Making best use of model evaluations to compute sensitivity indices. Comput. Phys. Commun. 145, 280–297.

Saquella, S., Laneve, G., Ferrari, A., 2022. A Cross-Correlation Phenology-Based Crop Fields Classification Using Sentinel-2 Time-Series, in: IGARSS 2022 - 2022 IEEE International Geoscience and Remote Sensing Symposium. IEEE, pp. 5660–5663. https://doi.org/10.1109/IGARSS46834.2022.9884724

Scheffler, D., Hollstein, A., Diedrich, H., Segl, K., Hostert, P., 2017. AROSICS: An automated and robust open-source image co-registration software for multi-sensor satellite data. Remote Sens. 9. https://doi.org/10.3390/rs9070676

Selva, M., Aiazzi, B., Butera, F., Chiarantini, L., Baronti, S., 2015. Hyper-Sharpening: A First Approach on SIM-GA Data. IEEE J. Sel. Top. Appl. Earth Obs. Remote Sens. 8, 3008–3024. https://doi.org/10.1109/JSTARS.2015.2440092

Sobol, I.M., 2001. Global sensitivity indices for nonlinear mathematical models and their Monte Carlo estimates. Math. Comput. Simul. 55, 271–280.

Sobol, I.M., 1993. Sensitivity analysis for non-linear mathematical models. Math. Model. Comput. Exp. 1, 407–414.

Vivone, G., Alparone, L., Chanussot, J., Dalla Mura, M., Garzelli, A., Licciardi, G.A., Restaino, R., Wald, L., 2015. A Critical Comparison Among Pansharpening Algorithms. IEEE Trans. Geosci. Remote Sens. 53, 2565–2586. https://doi.org/10.1109/TGRS.2014.2361734

Wan, Z., 2006. MODIS_LST_products_Users_guide_C4. Icess 1–33.

Wang, R., Gao, W., Peng, W., 2020. Downscale MODIS Land Surface Temperature Based on Three Different Models to Analyze Surface Urban Heat Island: A Case Study of Hangzhou. Remote Sens. 12, 2134. https://doi.org/10.3390/rs12132134

Wang, X., Shao, Z., Huang, X., Li, D., 2022. Spatiotemporal Temperature Fusion Based on a Deep Convolutional Network. Photogramm. Eng. Remote Sens. 88, 93–101. https://doi.org/10.14358/PERS.21-00023R2

Waske, B., Fauvel, M., Benediktsson, J.A., Chanussot, J., 2009. Machine learning techniques in remote sensing data analysis Kernel methods for remote sensing data analysis, in: Kernel Methods for Remote Sensing Data Analysis. Wiley, pp. 3–24. https://doi.org/10.1002/9780470748992.ch1

Weiss, M., Baret, F., Smith, G.J., Jonckheere, I., Coppin, P., 2004. Review of methods for in situ leaf area index (LAI) determination Part II. Estimation of LAI, errors and sampling. Agric. For. Meteorol. 121, 37–53. https://doi.org/10.1016/j.agrformet.2003.08.001

Weng, Q., Fu, P., Gao, F., 2014. Generating daily land surface temperature at Landsat resolution by fusing Landsat and MODIS data. Remote Sens. Environ. 145, 55–67. https://doi.org/10.1016/j.rse.2014.02.003

Xia, H., Chen, Y., Li, Y., Quan, J., 2019. Combining kernel-driven and fusion-based methods to generate daily high-spatial-resolution land surface temperatures. Remote Sens. Environ. 224, 259–274. https://doi.org/10.1016/j.rse.2019.02.006

Xie, Q., Zhou, M., Zhao, Q., Meng, D., Zuo, W., Xu, Z., 2019. Multispectral and Hyperspectral Image Fusion by MS/HS Fusion Net, in: Proceedings of the IEEE Computer Society Conference on Computer Vision and Pattern Recognition.

Xiong, X.J., Wenny, B.N., Barnes, W.L., 2009. Overview of NASA Earth Observing Systems Terra and Aqua moderate resolution imaging spectroradiometer instrument calibration algorithms and on-orbit performance. J. Appl. Remote Sens. 3, 32501–32525. https://doi.org/10.1117/1.3180864

Yang, Y., Cao, C., Pan, X., Li, X., Zhu, X., 2017. Downscaling Land Surface Temperature in an Arid Area by Using Multiple Remote Sensing Indices with Random Forest Regression. Remote Sens. 9, 789. https://doi.org/10.3390/rs9080789

Yebra, M., Dennison, P.E., Chuvieco, E., Riaño, D., Zylstra, P., Hunt, E.R., Danson, F.M., Qi, Y., Jurdao, S., 2013. A global review of remote sensing of live fuel moisture content for fire danger assessment: Moving towards operational products. Remote Sens. Environ. 136, 455–468. https://doi.org/10.1016/j.rse.2013.05.029

Yin, Z., Wu, P., Foody, G.M., Wu, Y., Liu, Z., Du, Y., Ling, F., 2021. Spatiotemporal Fusion of Land Surface Temperature Based on a Convolutional Neural Network. IEEE Trans. Geosci. Remote Sens. 59, 1808–1822. https://doi.org/10.1109/TGRS.2020.2999943

Yokoya, N., Grohnfeldt, C., Chanussot, J., 2017. Hyperspectral and Multispectral Data Fusion: A comparative review of the recent literature. IEEE Geosci. Remote Sens. Mag. 5, 29–56. https://doi.org/10.1109/MGRS.2016.2637824

Yokoya, N., Yairi, T., Iwasaki, A., 2011. Hyperspectral, multispectral, and panchromatic data fusion based on non-negative matrix factorization, in: IEEE WHISPERS. pp. 1–4.

Yoo, C., Im, J., Park, S., Cho, D., 2020. Spatial downscaling of MODIS land surface temperature: Recent research trends, challenges, and future directions. Korean J. Remote Sens. https://doi.org/10.7780/kjrs.2020.36.4.9

Yu, J., Fan, Y., Yang, J., Xu, N., Wang, Z., Wang, X., Huang, T., 2018. Wide Activation for Efficient and Accurate Image Super-Resolution.

Appendix 1: Formulas for a selection of vegetation indices adapted to PRISMA sensor.

List of selected spectral indices of interest and corresponding formulas specialized for the PRISMA channels.

Name	Formula	PRISMA channels
	Structure	
NDVI	(NIR-RED)/(NIR+RED)	$(B_{17} - B_{34})/(B_{17} + B_{34})$
MCARI	$[(R_{700} - R_{670})-0.2*(R_{700}-R_{550})]*R_{700}/R_{670}$	$[(B_{30} - B_{33})-0.2*(B_{30}-B_{47})]*B_{30}/B_{33}$
MSAVI	$[2*R_{800}+1-sqrt((2*R_{800}-1)\text{\textasciicircum}2-8*(R_{800}-R_{600}))]/2$	$[2*B_{20}+1-sqrt((2*B_{20}-1)^2-8*(B_{20}-B_{41}))]/2$
MTVI	$1.2*[1.2*(R_{800}-R_{550})-2.5*(R_{670}-R_{550})]$	$1.2*[1.2*(B_{20}-B_{47})-2.5*(B_{33}-B_{47})]$
OSAVI	$1.16*(R_{800}-R_{700})/(R_{800}+R_{670}+0.16)$	$1.16*(B_{20}-B_{30})/(B_{20}+B_{33}+0.16)$
SPVI	$0.4*[(3.7*(R_{800}-R_{670})-1.2*abs(R_{530}-R_{670})]$	$0.4*[(3.7*(B_{20}-B_{33})-1.2*abs(B_{49}-B_{33})]$
RDVI	$(R_{800}-R_{670})/(R_{800}+R_{670})^{0.5}$	$(B_{20}-B_{33})/(B_{20}+B_{33})^{0.5}$
	Chlorophyll	
CSI	R_{695}/R_{760}	B_{31}/B_{24}
Greenness Index	R_{554}/R_{677}	B_{47}/B_{33}
GM	R_{750}/R_{700}	B_{25}/B_{30}
NPQI	$(R_{415}-R_{435})/(R_{415}+R_{435})$	$(B_{65}-B_{62})/(B_{65}+B_{62})$
PRI	$(R_{570}-R_{531})/(R_{570}+R_{531})$	$(B_{45}-B_{50})/(B_{45}+B_{50})$
Red Edge Point	$700+40*(R_{rededge} - R_{670})/(R_{740}-R_{700})$; $R_{rededge} = (R_{670}+R_{780})/2$	$700+40*(B_{Bededge} - B_{33})/(B_{26}-B_{30})$; $B_{Bededge} = (B_{33}+B_{23})/2$
SR705	R_{750}/R_{705}	B_{25}/B_{30}
TCARI	$3*[(R_{700} - R_{670})-0.2*(R_{700}-R_{550})]*(R_{700}/R_{670})$	$3*[(B_{30} - B_{33})-0.2*(B_{30}-B_{47})]*(B_{30}/B_{33})$
TVI	$0.5\cdot[120*(R_{750}-R_{550})-200*(R_{670}-R_{550})]$	$0.5\cdot[120*(B_{25}-B_{47})-200*(B_{33}-B_{47})]$

Vogelmann Index	R_{740}/R_{720}	B_{26}/B_{28}
ZTM	R_{750}/R_{710}	B_{25}/B_{29}
SR	R_{675}/R_{700}	B_{33}/B_{30}
PSSR	R_{800}/R_{675}	B_{21}/B_{33}
LCI	$(R_{850}-R_{710})/(R_{850}+R_{680})$	$(B_{16}-B_{29})/(B_{16}+B_{32})$
MLO	R_{531}/R_{645}	B_{50}/B_{36}
MSR	$(R_{800}/R_{670}-1)/\mathrm{sqrt}(R_{800}/R_{670}+1)$	$(B_{20}/B_{33}-1)/(B_{20}+B_{33}+1)^{0.5}$

Carotenoids and Anthocyanin

ARI	$1/R_{550} - 1/R_{700}$	$1/B_{47} - 1/B_{30}$
CRI	$1/R_{510} - 1/R_{550}$	$1/B_{52} - 1/B_{47}$
PSSRc	R_{800}/R_{500}	B_{21}/B_{54}
SIPI	$(R_{800}-R_{445})/(R_{800}-R_{680})$	$(B_{20}-B_{61})/(B_{20}-B_{32})$

Leaf Water

DSWI	$(R_{802}+R_{547})/(R_{1657}+R_{682})$	$(B_{20}+B_{47})/(B_{103}+B_{32})$
LWVI	$(R_{1094}-R_{1205})/(R_{1094}+R_{1205})$	$(B_{155}-B_{145})/(B_{155}+B_{145})$
MSI	R_{1600}/R_{820}	B_{109}/B_{19}
NDWI	$(R_{860}-R_{1240})/(R_{860}+R_{1240})$	$(B_{15}-B_{142})/(B_{15}+B_{142})$
PWI	R_{970}/R_{900}	B_{168}/B_{11}
SRWI	R_{858}/R_{1240}	B_{15}/B_{142}

Dry matter

SWIRV1	$37.27*(R_{2210}+R_{2090})+26.27*(R_{2208}-R_{2090})-0.57$	$37.27*(B_{2210}+B_{2090})+26.27*(B_{2208}-B_{2090})-0.57$
CAI	$0.5*(R_{2015}+R_{2195})-R_{2106}$	$0.5*(B_{64}+B_{43})-B_{54}$
NDLI	$[(\log(R_{1094}))^{-1} - (\log(R_{1205}))^{-1}]/[(\log(R_{1094}))^{-1} + (\log(R_{1205}))^{-1}]$	$[(\log(B_{155}))^{-1} - (\log(B_{145}))^{-1}]/[(\log(B_{155}))^{-1} + (\log(B_{145}))^{-1}]$
NDNI	$[(\log(R_{1510}))^{-1} - (\log(R_{1680}))^{-1}]/$	$[(\log(B_{117}))^{-1} - (\log(B_{101}))^{-1}]/[(\log(B_{117}))^{-1} +$

	$[(\log(R_{1510}))^{-1} + (\log(R_{1680}))^{-1}]$	$(\log(B_{101}))^{-1}]$
BGI	R_{450}/R_{550}	B_{60}/B_{47}
BRI	R_{450}/R_{690}	B_{60}/B_{31}
RGI	R_{690}/R_{550}	B_{31}/B_{47}
SRPI	R_{430}/R_{680}	B_{63}/B_{32}
NPCI	$(R_{680}-R_{430})/(R_{680}+R_{430})$	$(B_{32}-B_{63})/(B_{32}+B_{63})$
PSRI	$(R_{680}-R_{500})/R_{750}$	$(B_{32}-B_{53})/B_{25}$

Fluorescence

CUR	$(R_{675}*R_{550})/(R_{683})^2$	$(B_{33}*B_{47})/(B_{32})^2$
LIC	$(R_{800}-R_{680})/(R_{800}+R_{680})$	$(B_{21}-B_{32})/(B_{21}+B_{32})$

Values of bands equal or higher than 66 refer to the numbering of the PRISMA SWIR sensor.
R refers to the central wavelength of the narrow band reflectance channel and B refers to the PRISMA spectral band

Appendix 2: PRISMA spectral channels.

Numbering of the bands as they appear in the PRISMA hdf5 file.

VNIR bands				SWIR bands					
Num.	λ	Num.	λ	Num.	λ	Num.	λ	Num.	λ
1	0	51	519.5438	1	2497.116	61	2044.681	121	1469.931
2	0	52	512.0464	2	2490.219	62	2036.261	122	1459.316
3	0	53	504.5117	3	2483.793	63	2027.727	123	1449.189
4	977.3654	54	497.0587	4	2477.055	64	2019.321	124	1438.466
5	967.0267	55	489.7949	5	2469.627	65	2010.661	125	1427.375
6	956.2715	56	482.5482	6	2463.03	66	2002.111	126	1416.537
7	944.6273	57	475.3189	7	2456.586	67	1993.548	127	1405.627

8	934.1121	58	468.0984	8	2449.142	68	1984.853	128	1394.754
9	923.9502	59	460.7318	9	2442.403	69	1976.013	129	1383.28
10	913.4451	60	453.3895	10	2435.544	70	1967.342	130	1372.912
11	902.8016	61	446.0147	11	2428.668	71	1958.624	131	1361.053
12	892.0809	62	438.6569	12	2421.237	72	1949.901	132	1349.788
13	881.4561	63	431.3347	13	2414.357	73	1941.111	133	1339.129
14	870.7426	64	423.7848	14	2407.605	74	1932.26	134	1328.299
15	859.9731	65	415.839	15	2400.036	75	1923.386	135	1317.257
16	849.21	66	406.9934	16	2393.039	76	1914.302	136	1306.218
17	838.5272			17	2386.062	77	1904.935	137	1295.422
18	827.9195			18	2378.771	78	1896.091	138	1284.488
19	817.311			19	2371.552	79	1887.081	139	1273.496
20	806.7111			20	2364.595	80	1878.743	140	1262.532
21	796.127			21	2357.294	81	1868.173	141	1250.98
22	785.6596			22	2349.792	82	1859.559	142	1240.215
23	775.2735			23	2342.823	83	1850.554	143	1229.185
24	764.8565			24	2335.526	84	1841.326	144	1217.864
25	754.4696			25	2327.824	85	1832.027	145	1207.274
26	744.1495			25	2320.896	86	1822.441	146	1196.339

27	733.9552			27	2313.201	87	1813.051	147	1185.588
28	723.8799			28	2305.723	88	1803.59	148	1174.714
29	713.7269			29	2298.609	89	1793.953	149	1163.676
30	703.737			30	2290.827	90	1784.717	150	1152.65
31	694.1284			31	2283.493	91	1775.118	151	1142.07
32	684.1373			32	2276.054	92	1765.513	152	1131.305
33	674.4644			33	2268.288	93	1755.833	153	1120.676
34	664.8941			34	2260.867	94	1746.219	154	1109.889
35	655.4188			35	2253.11	95	1736.488	155	1099.278
36	645.9638			36	2245.449	96	1726.652	156	1088.761
37	636.6763			37	2237.904	97	1716.859	157	1078.216
38	627.7784			38	2230.008	98	1707.095	158	1067.795
39	618.72			39	2222.426	99	1697.294	159	1057.574
40	609.9582			40	2214.625	100	1687.427	160	1047.675
41	601.0144			41	2206.843	101	1677.319	161	1037.988
42	592.339			42	2199.135	102	1667.185	162	1029.344
43	583.8441			43	2191.1	103	1656.933	163	1018.536
44	575.4868			44	2183.42	104	1647.232	164	1008.644
45	567.2061			45	2175.344	105	1637.092	165	998.9082
46	559.0203			46	2167.485	106	1627.021	166	988.9179

47	550.9146			47	2159.564	107	1616.834	167	979.224
48	542.8851			48	2151.386	108	1606.491	168	969.8449
49	535.0526			49	2143.466	109	1596.245	169	959.974
50	527.3053			50	2135.51	110	1585.86	170	951.4014
				51	2127.337	111	1575.627	171	943.3579
				52	2119.231	112	1565.369	172	0
				53	2111.039	113	1554.817	173	0
				54	2102.821	114	1544.226		
				55	2094.625	115	1533.776		
				56	2086.382	116	1523.222		
				57	2077.992	117	1512.633		
				58	2069.796	118	1502.024		
				59	2061.379	119	1491.429		
				60	2053.008	120	1480.842		

END OF THE DOCUMENT